32. A. N. Kapanidis *et al.*, *Science* **314**, 1144 (2006).
33. M. Gotte, G. Maier, H. J. Gross, H. Heumann, *J. Biol. Chem.* **273**, 10139 (1998).
34. H. Huang, R. Chopra, G. L. Verdine, S. C. Harrison, *Science* **282**, 1669 (1998).
35. J. Ren *et al.*, *Nat. Struct. Biol.* **2**, 293 (1995).
36. Y. Quan, C. Liang, P. Inouye, M. A. Wainberg, *Nucleic Acids Res.* **26**, 5692 (1998).
37. L. Ratner *et al.*, *Nature* **313**, 277 (1985).
38. P. H. von Hippel, O. G. Berg, *J. Biol. Chem.* **264**, 675 (1989).
39. H. Kabata *et al.*, *Science* **262**, 1561 (1993).
40. M. Guthold *et al.*, *Biophys. J.* **77**, 2284 (1999).
41. P. C. Blainey, A. M. van Oijen, A. Banerjee, G. L. Verdine, X. S. Xie, *Proc. Natl. Acad. Sci. U.S.A.* **103**, 5752 (2006).
42. J. Elf, G. W. Li, X. S. Xie, *Science* **316**, 1191 (2007).
43. K. B. Hall, L. W. McLaughlin, *Biochemistry* **30**, 10606 (1991).
44. N. Sugimoto, S. Nakano, M. Yoneyama, K. Honda, *Nucleic Acids Res.* **24**, 4501 (1996).
45. G. J. Klarmann, C. A. Schauber, B. D. Preston, *J. Biol. Chem.* **268**, 9793 (1993).

46. This work is supported in part by NIH (GM 068518 to X.Z.) and the Intramural Research Program of the Center for Cancer Research, National Cancer Institute (to S.F.J.L.G.). X.Z. is a Howard Hughes Medical Institute investigator. E.A.A. is a Jane Coffin Childs postdoctoral fellow. Nevirapine was provided through the AIDS Research and Reference Reagent Program of NIH.

Supporting Online Material

www.sciencemag.org/cgi/content/full/322/5904/1092/DC1
Materials and Methods
Figs. S1 to S12
References

11 July 2008; accepted 24 September 2008
10.1126/science.1163108

Batf3 Deficiency Reveals a Critical Role for CD8α$^+$ Dendritic Cells in Cytotoxic T Cell Immunity

Kai Hildner,[1,2] Brian T. Edelson,[1] Whitney E. Purtha,[3] Mark Diamond,[1] Hirokazu Matsushita,[1] Masako Kohyama,[1,2] Boris Calderon,[1] Barbara U. Schraml,[1] Emil R. Unanue,[1] Michael S. Diamond,[1,3] Robert D. Schreiber,[1] Theresa L. Murphy,[1] Kenneth M. Murphy[1,2]*

Although in vitro observations suggest that cross-presentation of antigens is mediated primarily by CD8α$^+$ dendritic cells, in vivo analysis has been hampered by the lack of systems that selectively eliminate this cell lineage. We show that deletion of the transcription factor *Batf3* ablated development of CD8α$^+$ dendritic cells, allowing us to examine their role in immunity in vivo. Dendritic cells from *Batf3*$^{-/-}$ mice were defective in cross-presentation, and *Batf3*$^{-/-}$ mice lacked virus-specific CD8$^+$ T cell responses to West Nile virus. Importantly, rejection of highly immunogenic syngeneic tumors was impaired in *Batf3*$^{-/-}$ mice. These results suggest an important role for CD8α$^+$ dendritic cells and cross-presentation in responses to viruses and in tumor rejection.

During antigen cross-presentation (*1*), antigens generated in one cell are presented by major histocompatibility complex (MHC) class I molecules of a second cell. It remains unclear whether all antigen presenting cells (APCs) use cross-presentation and whether this pathway plays a role in immune responses in vivo (*2*). Dendritic cells (DCs) are a heterogeneous group of APCs with two major subsets, plasmacytoid dendritic cells (pDCs) and conventional CD11c$^+$ dendritic cells (cDCs) (*3*). Subsets of cDCs include CD8α$^+$, CD4$^+$, and CD8α$^-$CD4$^-$ populations that may exert distinct functions in immune responses. Evidence has suggested that CD8α$^+$ cDCs are important for cross-presentation during infections but has its basis in ex vivo analysis (*4*–*6*) or in vitro antigen loading (*7*). Evidence both for and against a role for cross-presentation in responses against tumors has been reported (*8*–*10*).

Attempts have been made to study the in vivo role of DCs by selective depletion. Diphtheria toxin treatment can deplete all CD11c^{hi} cells in one transgenic mouse model (*11*) but affects splenic macrophages and activated CD8$^+$ T cells (*12*). Gene targeting of transcription factors (e.g., *Irf2*, *Irf4*, *Irf8*, *Stat3*, and *Id2*) has caused broad defects in several DC subsets, T cells, and macrophages (*13*). To identify genes regulating DC development, we performed global gene expression analysis across many tissues and immune cells (fig. S1A). *Batf3* (also known as *Jun dimerization protein p21SNFT*) (*14*) was highly expressed in cDCs, with low to absent expression in other immune cells and nonimmune tissues. Thus, we generated *Batf3*$^{-/-}$ mice that lack expression of the Batf3 protein (fig. S1, B to D).

In spleens of *Batf3*$^{-/-}$ mice, we found a selective loss of CD8α$^+$ cDCs, without abnormalities in other hematopoietic cell types or architecture (Fig. 1 and figs. S2 to S14). CD8α$^+$ cDCs coexpress DEC205, CD24, and low levels of CD11b (*3*, *15*). *Batf3*$^{-/-}$ mice lacked splenic CD11c^{hi}CD8α$^+$DEC205$^+$ cells (Fig. 1A), showed a loss of CD11c^{hi}CD11b^{dull} cells and CD11c^{hi}CD8α$^+$CD24$^+$ cells (Fig. 1B), but had normal populations of CD4$^+$ and CD8α$^-$CD4$^-$ cDC subsets (Fig. 1B). Lymph nodes and thymi of *Batf3*$^{-/-}$ mice lacked CD8α$^+$ DCs but had normal distributions of CD8α$^-$CD11c$^+$ cells (Fig. 1C). DEC205^{int} and DEC205^{hi} DCs were present in lymph nodes draining the skin of *Batf3*$^{-/-}$ mice (Fig. 1C) and showed normal migration from skin to lymph node after topical application of fluorescein-5-isothiocyanate (fig. S3A). *Batf3*$^{-/-}$ mice had normal development of pDCs (CD11c^{int}CD11b$^-$B220$^+$) (fig. S3B), interstitial DCs of pancreatic islets (CD11c$^+$CD8α$^-$) (fig. S3, C and D), monocytes, neutrophils (fig. S3E), and SIGN-R1$^+$ marginal zone and MOMA-1$^+$ metallophilic macrophages (Fig. 2A). CD8α$^+$ cDCs developed normally in heterozygous *Batf3*$^{+/-}$ mice (fig. S4A) and were absent in *Rag2*$^{-/-}$ *Batf3*$^{-/-}$ mice (fig. S4B).

This loss of CD8α$^+$ cDCs could result from a cell-autonomous hematopoietic defect or a cell-extrinsic requirement for *Batf3*. To distinguish these possibilities, we generated chimeras in which CD45.2$^+$ *Batf3*$^{+/+}$ or CD45.2$^+$ *Batf3*$^{-/-}$ bone marrow (BM) was transplanted into lethally irradiated CD45.1$^+$CD45.2$^+$ recipients (Fig. 2B). Upon reconstitution (fig. S5A), we found CD8α$^+$ cDCs developed only from *Batf3*$^{+/+}$ donor BM cell (Fig. 2B), indicating a cell-intrinsic hematopoietic defect in *Batf3*$^{-/-}$ mice.

Treatment of mice with fms-like tyrosine kinase 3 (flt3) ligand–Fc (FL-Fc) increased the numbers of CD8α$^+$ cDCs, CD8α$^-$ cDCs, and pDCs in *Batf3*$^{+/+}$ mice but failed to increase the number of CD8α$^+$ cDCs in *Batf3*$^{-/-}$ mice (Fig. 2C). In vitro culture of BM with FL generates cell populations corresponding to pDCs (CD11c$^+$CD45RA$^+$) and cDCs (CD11c$^+$CD45RA$^-$) (*3*, *16*) (Fig. 2D). These in vitro–derived cDCs do not express CD8α or CD4 but contain a CD24$^+$Sirp-α$^{lo\text{-}int}$ population corresponding to CD8α$^+$ cDC (*16*). *Batf3*$^{+/+}$ or *Batf3*$^{-/-}$ BM cells treated with FL produced similar ratios of pDCs and cDCs (Fig. 2D and fig. S5B). However, *Batf3*$^{-/-}$ BM generated far fewer CD24$^+$ Sirp-α$^-$ cells compared with *Batf3*$^{+/+}$ BM (Fig. 2D), corresponding to loss of CD8α$^+$ cDCs. Lastly, DCs generated from *Batf3*$^{-/-}$ BM were selectively deficient in Toll-like receptor (TLR) 3-induced interleukin (IL)-12 production (fig. S5C), a specific feature of CD8α$^+$ cDCs (*16*). Similarly, CD11c$^+$ cDCs from the spleens of *Batf3*$^{-/-}$ mice were selectively deficient in TLR3-induced IL-12 production but had normal responses to TLR4 and TLR9 ligands (fig. S6A).

We next tested whether APCs from *Batf3*$^{-/-}$ mice could prime CD4$^+$ and CD8$^+$ T cell responses. Similar proliferative responses of OT-II transgenic CD4$^+$ T cells (*17*) occurred with soluble ovalbumin presented by *Batf3*$^{+/+}$ and *Batf3*$^{-/-}$ cDCs (fig. S6B). However, *Batf3*$^{-/-}$ cDCs were defective in an assay for cross-presentation of cellular antigen to CD8$^+$ T cells (*2*, *18*) (Fig. 3A). OT-I T cells proliferated in response to *Batf3*$^{+/+}$ cDCs cocultured with ovalbumin-loaded cells but failed to proliferate in response to *Batf3*$^{-/-}$ cDCs in this assay.

[1]Department of Pathology and Immunology, Washington University School of Medicine, 660 South Euclid Avenue, St. Louis, MO 63110, USA. [2]Howard Hughes Medical Institute, Washington University School of Medicine, 660 South Euclid Avenue, St. Louis, MO 63110, USA. [3]Departments of Medicine and Molecular Microbiology, 660 South Euclid Avenue, St. Louis, MO 63110, USA.

*To whom correspondence should be addressed. E-mail: kmurphy@wustl.edu

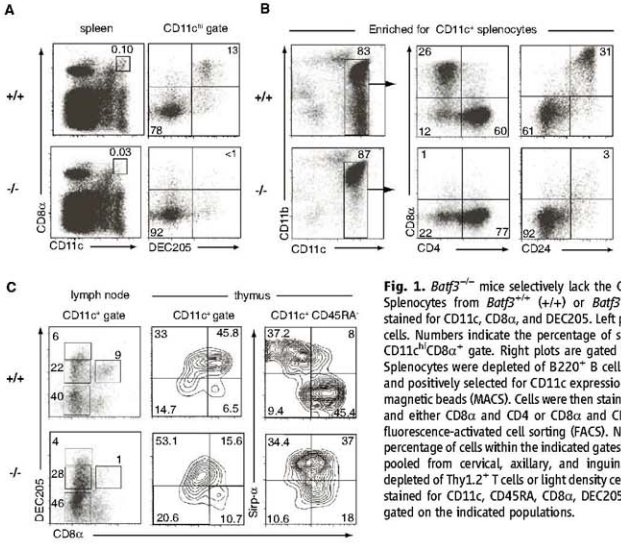

Fig. 1. *Batf3*$^{-/-}$ mice selectively lack the CD8α$^+$ DC subset. **(A)** Splenocytes from *Batf3*$^{+/+}$ (+/+) or *Batf3*$^{-/-}$ (–/–) mice were stained for CD11c, CD8α, and DEC205. Left plots are gated on live cells. Numbers indicate the percentage of splenocytes within the CD11c^{hi}CD8α$^+$ gate. Right plots are gated on CD11c^{hi} cells. **(B)** Splenocytes were depleted of B220$^+$ B cells and Thy1.2$^+$ T cells and positively selected for CD11c expression by antibody-coated magnetic beads (MACS). Cells were then stained for CD11c, CD11b, and either CD8α and CD4 or CD8α and CD24 and analyzed by fluorescence-activated cell sorting (FACS). Numbers represent the percentage of cells within the indicated gates. **(C)** Lymph node cells pooled from cervical, axillary, and inguinal lymph nodes and depleted of Thy1.2$^+$ T cells or light density cells of the thymus were stained for CD11c, CD45RA, CD8α, DEC205, or Sirp-α. Plots are gated on the indicated populations.

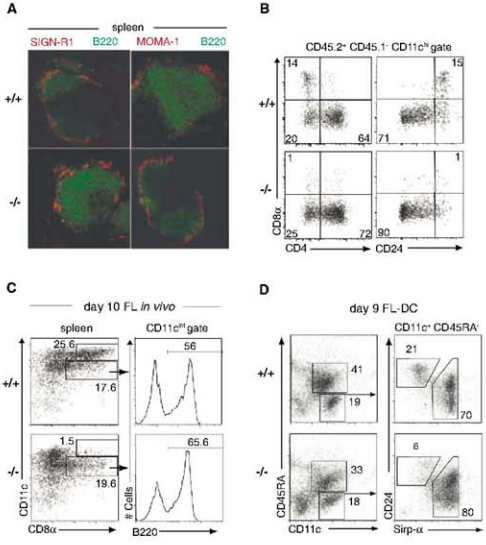

Fig. 2. Functional loss of CD8α$^+$ cDCs in *Batf3*$^{-/-}$ mice is cell-intrinsic to the hematopoietic system. **(A)** Frozen sections from *Batf3*$^{+/+}$ (+/+) or *Batf3*$^{-/-}$ (–/–) mice were stained for B220 (green) and SIGN-R1 (red) expression (left) or for B220 (green) and MOMA-1 (red) (right). **(B)** Irradiated F1(B6.SJL/129SvEv) mice (CD45.1$^+$CD45.2$^+$) were reconstituted with 2 × 10^7 bone marrow cells from *Batf3*$^{+/+}$ (+/+) or *Batf3*$^{-/-}$ (–/–) CD45.1$^-$CD45.2$^+$ mice. After 10 weeks, donor cells (CD45.1$^-$CD45.2$^+$) were analyzed for CD11c, CD8α, CD4, and CD24 expression. Shown are plots for CD8α and CD4 (left) or CD8α and CD24 (right) gated on CD11c^{hi} donor-derived cells. Numbers represent the percentage of cells within the indicated gates. **(C)** *Batf3*$^{+/+}$ (+/+) or *Batf3*$^{-/-}$ (–/–) mice were treated intraperitoneally with 10 μg FL-Fc. After 10 days, splenocytes were enriched for CD11c$^+$ by MACS and stained for CD11c, CD8α, and B220. Plots are gated on live cells (left) or CD11c^{hi}CD8α$^+$ cells (right). Numbers represent the percentage of cells within the indicated gates. **(D)** *Batf3*$^{+/+}$ (+/+) or *Batf3*$^{-/-}$ (–/–) BM cells were cultured in FL (20 ng/ml) for 9 days, and nonadherent cells were analyzed for CD11c, CD45RA, CD24, and Sirp-α expression. Plots are gated on live cells (left) or CD11c$^+$ CD45RA$^-$ cells (right).

We examined responses of *Batf3*$^{-/-}$ mice to West Nile virus (WNV) (*19*, *20*) (fig. S6). *Batf3*$^{-/-}$ mice showed normal WNV-specific antibody responses (Fig. 3B) and memory B cell (fig. S6C) and CD4$^+$ T cell responses (fig. S6D) but had a dramatic reduction in WNV-specific CD8$^+$ T cell responses (Fig. 3C) and in vivo cytotoxic T lymphocyte (CTL) killing of WNV peptide–loaded target cells (fig. S7, A and B). *Batf3*$^{-/-}$ mice lacked WNV-specific memory CD8$^+$ T cells and had impaired formation of CD8$^+$CD44^{hi}CD62L^{low} cells (fig. S7). Adoptive transfer of *Batf3*$^{-/-}$ CD8$^+$ T cells into *Rag2*$^{-/-}$ mice generated normal WNV-specific CD8$^+$ T cell response (Fig. 3D), but adoptive transfer of *Batf3*$^{+/+}$ CD8$^+$ T cells into *Batf3*$^{-/-}$ *Rag2*$^{-/-}$ mice generated an impaired WNV-specific CD8$^+$ T cell response (fig. S7C). This shows that impaired WNV-specific CTL responses in *Batf3*$^{-/-}$ mice results from a defect of DCs rather than CD8$^+$ T cells.

We challenged *Batf3*$^{+/+}$ and *Batf3*$^{-/-}$ mice with syngeneic fibrosarcomas that normally are rapidly rejected in a CD4$^+$ and CD8$^+$ T cell–dependent manner (*21*, *22*) (fig. S8A). Two independent fibrosarcomas were rapidly rejected by *Batf3*$^{+/+}$ mice but grew progressively in *Rag2*$^{-/-}$ mice and *Batf3*$^{-/-}$ mice (Fig. 4A and fig. S8, B and C). Moreover, *Batf3*$^{-/-}$ mice failed to develop tumor-specific CTLs (Fig. 4B). Tumor-infiltrating CD8$^+$ T cells, but not CD4$^+$ T cells, were significantly reduced in *Batf3*$^{-/-}$ mice (Fig. 4C). The failure of *Batf3*$^{-/-}$ mice to reject these tumors was not due to defective natural killer cell development or function (figs. S2B and S9, A to C). We considered whether *Batf3*$^{-/-}$ T cells have an intrinsic dysfunction because overexpression studies had suggested *Batf3* might affect IL-2 transcription (*14*). Although *Batf3* overexpression reduces IL-2 reporter activity in Jurkat T cells (fig. S10B), *Batf3*$^{-/-}$ CD4$^+$ T cells showed normal IL-2 production (fig. S10D) and normal T helper cell (T_H) T_H1, T_H2, and T_H17 differentiation (figs. S10, C to E, and S11B). Lastly, *Batf3*$^{-/-}$ CD8$^+$ T cells showed normal allospecific effector responses (fig. S11A) and cytokine production (fig. S11B).

Other DC subsets may cross-present, although less efficiently than CD8α$^+$ DCs (*23*–*26*), suggesting there may be residual cross-presentation capacity in *Batf3*$^{-/-}$ mice. We therefore challenged mice by using reduced tumor-cell numbers, which might allow effective responses in the setting of reduced cross-presentation (fig. S8). Whereas 10^4

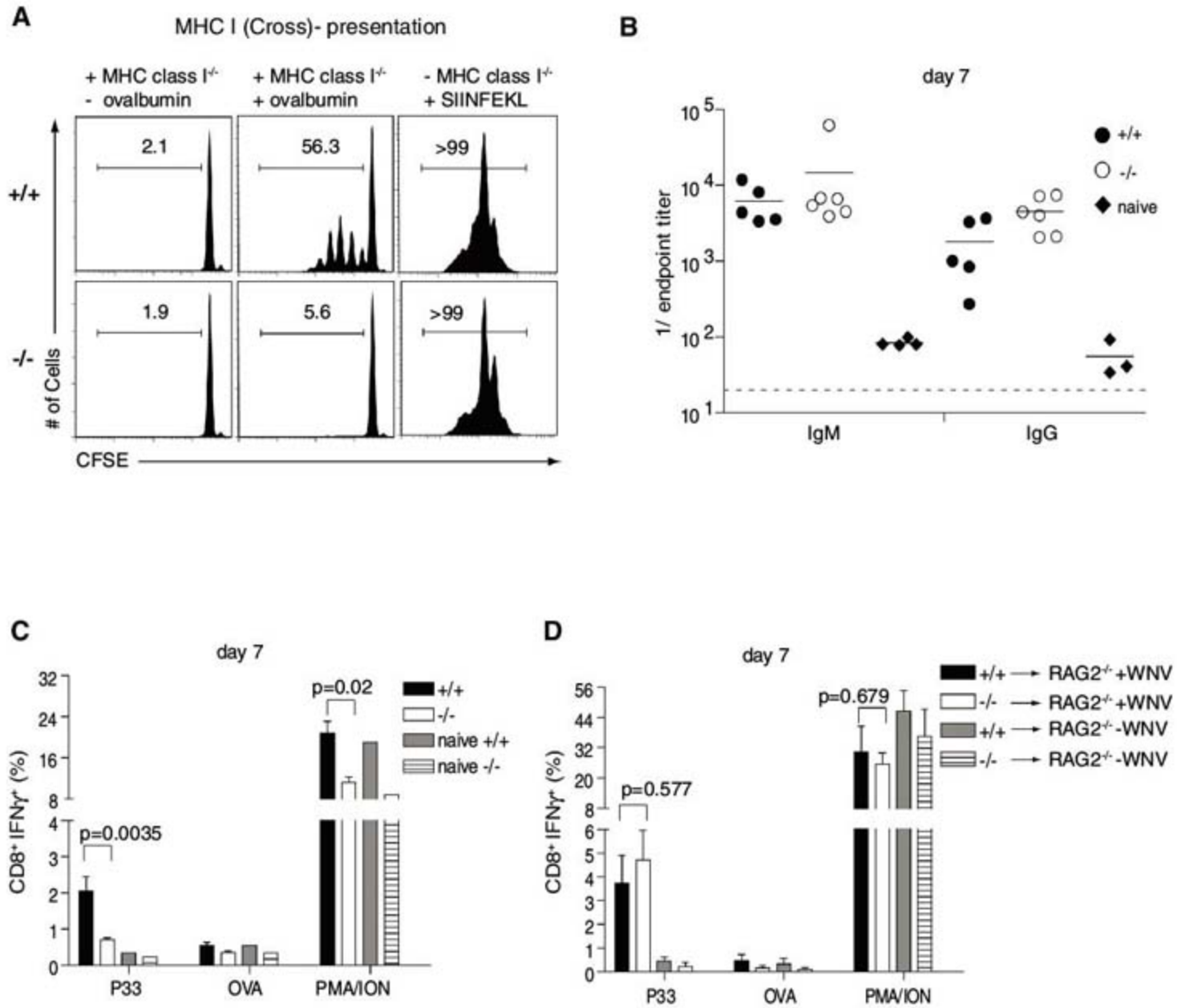

Fig. 3. Lack of cross-presentation and antiviral CTL responses in *Batf3*$^{-/-}$ mice. (**A**) *Batf3*$^{+/+}$ (+/+) or *Batf3*$^{-/-}$ (–/–) splenocytes were depleted of B220$^+$ B cells and Thy1.2$^+$ T cells, enriched for CD11c by MACS, and cultured with irradiated MHC class I$^{-/-}$ splenocytes as indicated that were either untreated (–ovalbumin), pulsed with 10 mg/ml soluble ovalbumin (+ovalbumin), or cultured with 1 μM Ser-Ile-Ile-Asn-Phe-Glu-Lys-Leu (SIINFEKL) peptide. Carboxyfluorescein succinimidyl ester (CFSE)-labeled CD45.1$^+$ OT-I T cells were cultured with these cells, and proliferation was determined by FACS after 60 hours. Single-color histograms of CD8$^+$CD45.1$^+$ OT-I T cells show the percentage of cells in the indicated gates. (**B**) *Batf3*$^{+/+}$ (+/+) or *Batf3*$^{-/-}$ (–/–) mice were infected with 100 plaque-forming units (PFUs) of WNV. On day 7, isotype-specific anti-WNV E protein titers were measured. Horizontal lines represent mean titers and dotted line represents limit of detection. (**C**) *Batf3*$^{+/+}$ (+/+) or *Batf3*$^{-/-}$ (–/–) mice were infected with 100 PFUs of WNV or left uninfected. After 7 days, splenocytes were stimulated in vitro with the WNV-specific NS4B peptide (P33), OVA peptide, or phorbol 12-myristate 13-acetate (PMA)/ionomycin as described. CD8$^+$ T cells were analyzed for expression of intracellular interferon γ (IFN-γ). Data shown are mean ± SEM (n = 9 to 10). (**D**) *Batf3*$^{+/+}$ (+/+) or *Batf3*$^{-/-}$ (–/–) CD8$^+$ T cells were transferred intravenously into *Rag2*$^{-/-}$ recipients. After 24 hours, mice were infected with 100 PFU of WNV (+WNV) or left uninfected (–WNV). After 7 days, splenocytes were harvested and analyzed as described in (C). Data shown are mean ± SEM (n = 6). Three independently performed experiments yielded similar results.

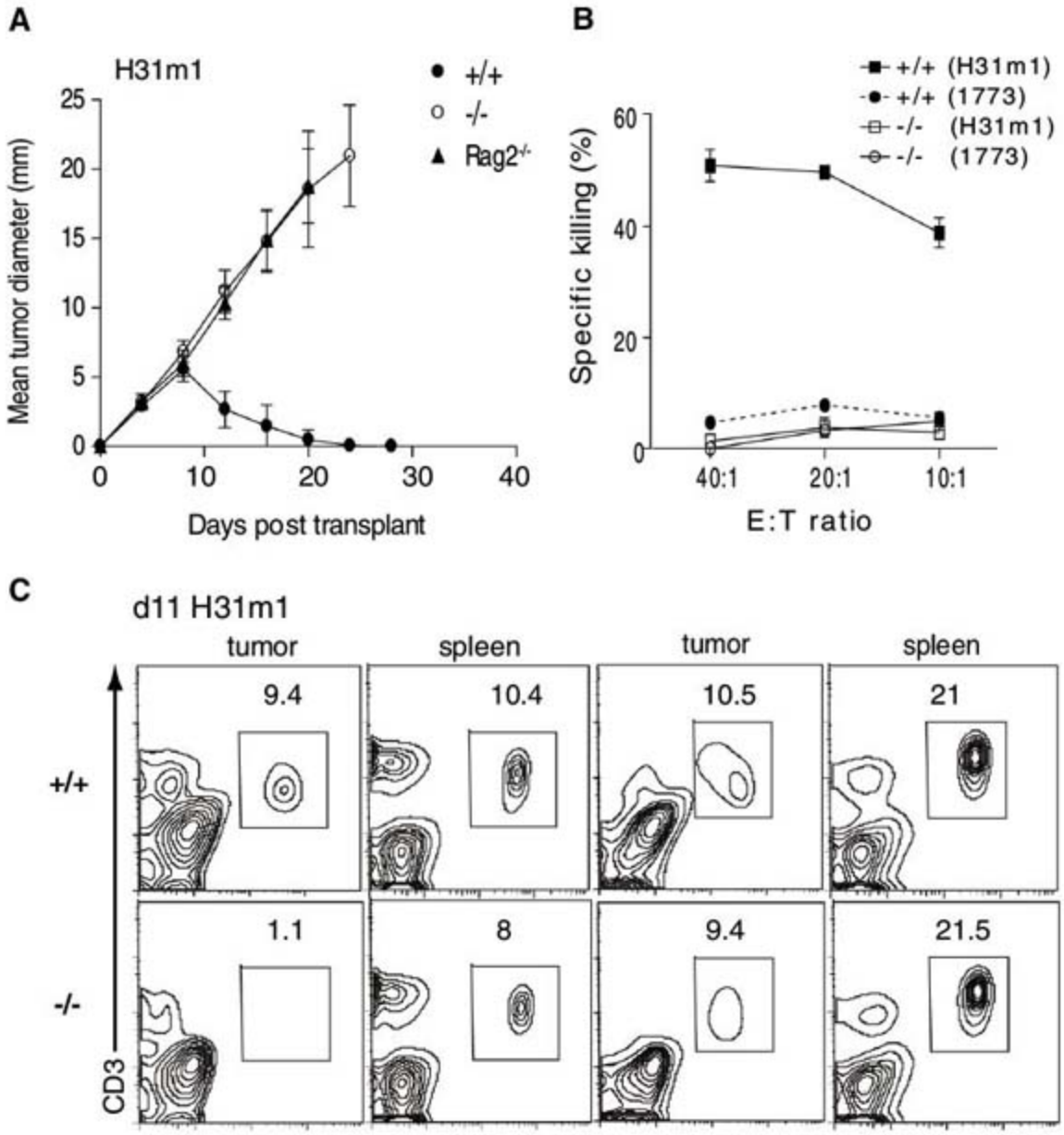

Fig. 4. Lack of tumor rejection in *Batf3*$^{-/-}$ mice. (**A**) 10^6 H31m1 fibrosarcoma cells were injected subcutaneously into *Batf3*$^{+/+}$ (solid circles), *Batf3*$^{-/-}$ (open circles), or *Rag2*$^{-/-}$ (triangles) mice, and tumor diameter (±SD) ($n = 10$) was measured. (**B**) Mice were treated as in (A). After 9 days, splenocytes were harvested and cocultured with IFN-γ pretreated, irradiated H31m1 tumor cells. After 5 days, a CTL killing assay using ^{51}Cr-labeled H31m1 or 1773 tumor cells as target cells was performed. Shown is specific killing activity as described in (*30*). (**C**) Tumors and spleens from mice treated as in (A) were removed on day 11, and cells analyzed by FACS. Plots are gated on live CD45.2$^+$ cells and show CD3, CD8α, and CD4 expression. Numbers represent the percentage of cells within the indicated gate. Results are representative of at least three mice per group.

and 10^5 tumor cells grew in all *Rag2*$^{-/-}$ mice, some *Batf3*$^{-/-}$ mice controlled this lower tumor burden (fig. S8, D and E) and developed a tumor-specific CTL response (fig. S8F). Whereas adoptive transfer of wild-type DCs led to partial control of tumor growth in *Batf3*$^{-/-}$ mice, transfer of *Batf3*$^{-/-}$ DCs did not (fig. S12).

Subsets of cDCs have recently been described with functional similarities to CD8α$^+$ cDCs. Migratory Langerin$^+$ dermal and lung DC subsets express DEC205$^+$ and CD103$^+$ and, like CD8α$^+$ cDCs, are CD11b$^{lo/-}$ (*27*, *28*). CD8α$^+$ cDC and migratory CD103$^+$ DC populations share the distinctive properties of TLR3 responsiveness (*27*) and capacity for cross-presentation (*26*), further supporting the idea that these CD103$^+$ subsets may be related. In spleen, CD103 is coexpressed with CD8α on cDCs (fig. S13A) (*29*) and selectively expressed by the "CD8α equivalent" CD24$^+$Sirp-α$^{lo\text{-}int}$ cDC subset derived from FL-treated *Batf3*$^{+/+}$ BM (fig. S13C), but is not expressed by *Batf3*$^{-/-}$ splenic cDCs (fig. S13B) or FL-treated *Batf3*$^{-/-}$ BM cells. This suggests that CD103-expressing cDCs may require *Batf3*. In agreement, *Batf3*$^{-/-}$ mice showed a reduced number of CD103-expressing DEC205$^+$CD8α$^-$CD11b$^{lo/-}$ dermal DCs in skin-draining lymph nodes (fig. S14).

This study describes a transcription factor that controls development of CD8α$^+$ cDCs. *Batf3*$^{-/-}$ mice exhibit impaired antigen cross-presentation, impaired CTL responses against viral infection, and impaired responses to tumor challenge. These results suggest an important role for in vivo cross-presentation in CTL responses and provide support for therapeutic approaches that use CD8α$^+$ cDCs for the induction of effective immune responses.

References and Notes

1. M. J. Bevan, *J. Exp. Med.* **143**, 1283 (1976).
2. J. M. den Haan, S. M. Lehar, M. J. Bevan, *J. Exp. Med.* **192**, 1685 (2000).
3. K. Shortman, S. H. Naik, *Nat. Rev. Immunol.* **7**, 19 (2007).
4. R. S. Allan *et al.*, *Science* **301**, 1925 (2003).
5. G. T. Belz *et al.*, *J. Immunol.* **172**, 1996 (2004).
6. G. T. Belz, K. Shortman, M. J. Bevan, W. R. Heath, *J. Immunol.* **175**, 196 (2005).
7. O. Schulz *et al.*, *Nature* **433**, 887 (2005).
8. A. Y. Huang *et al.*, *Science* **264**, 961 (1994).
9. A. F. Ochsenbein *et al.*, *Nature* **411**, 1058 (2001).
10. M. C. Wolkers, G. Stoetter, F. A. Vyth-Dreese, T. N. Schumacher, *J. Immunol.* **167**, 3577 (2001).
11. S. Jung *et al.*, *Immunity* **17**, 211 (2002).
12. H. C. Probst *et al.*, *Clin. Exp. Immunol.* **141**, 398 (2005).
13. M. Zenke, T. Hieronymus, *Trends Immunol.* **27**, 140 (2006).
14. M. Iacobelli, W. Wachsman, K. L. McGuire, *J. Immunol.* **165**, 860 (2000).
15. D. Dudziak *et al.*, *Science* **315**, 107 (2007).
16. S. H. Naik *et al.*, *J. Immunol.* **174**, 6592 (2005).
17. M. J. Barnden, J. Allison, W. R. Heath, F. R. Carbone, *Immunol. Cell Biol.* **76**, 34 (1998).
18. N. S. Wilson *et al.*, *Nat. Immunol.* **7**, 165 (2006).
19. M. S. Diamond, B. Shrestha, A. Marri, D. Mahan, M. Engle, *J. Virol.* **77**, 2578 (2003).
20. E. M. Sitati, M. S. Diamond, *J. Virol.* **80**, 12060 (2006).
21. V. Shankaran *et al.*, *Nature* **410**, 1107 (2001).
22. G. P. Dunn *et al.*, *Nat. Immunol.* **6**, 722 (2005).
23. M. L. Lin, Y. Zhan, J. A. Villadangos, A. M. Lew, *Immunol. Cell Biol.* **86**, 353 (2008).
24. G. T. Belz *et al.*, *Proc. Natl. Acad. Sci. U.S.A.* **101**, 8670 (2004).
25. J. Waithman *et al.*, *J. Immunol.* **179**, 4535 (2007).
26. M. L. del Rio, J. I. Rodriguez-Barbosa, E. Kremmer, R. Forster, *J. Immunol.* **178**, 6861 (2007).
27. S. S. Sung *et al.*, *J. Immunol.* **176**, 2161 (2006).
28. L. S. Bursch *et al.*, *J. Exp. Med.* **204**, 3147 (2007).
29. A. D. Edwards *et al.*, *J. Immunol.* **171**, 47 (2003).
30. Materials and methods are available as supporting material on *Science* Online.

31. This work was supported by the Howard Hughes Medical Institute (K.M.M.), the Emmy Noether Program of the German Research Foundation (K.H.), and a Burroughs Wellcome Fund Career Award for Medical Scientists (B.T.E.).

Supporting Online Material

www.sciencemag.org/cgi/content/full/322/5904/1097/DC1
Materials and Methods
Figs. S1 to S14
References

5 August 2008; accepted 8 October 2008
10.1126/science.1164206

Del-1, an Endogenous Leukocyte-Endothelial Adhesion Inhibitor, Limits Inflammatory Cell Recruitment

Eun Young Choi,[1*] Emmanouil Chavakis,[2*] Marcus A. Czabanka,[3†] Harald F. Langer,[1†] Line Fraemohs,[4] Matina Economopoulou,[5] Ramendra K. Kundu,[6] Alessia Orlandi,[2] Ying Yi Zheng,[1] DaRue A. Prieto,[7] Christie M. Ballantyne,[8] Stephanie L. Constant,[9] William C. Aird,[10] Thalia Papayannopoulou,[11] Carl G. Gahmberg,[12] Mark C. Udey,[13] Peter Vajkoczy,[3] Thomas Quertermous,[6] Stefanie Dimmeler,[2] Christian Weber,[4] Triantafyllos Chavakis[1‡]

Leukocyte recruitment to sites of infection or inflammation requires multiple adhesive events. Although numerous players promoting leukocyte-endothelial interactions have been characterized, functionally important endogenous inhibitors of leukocyte adhesion have not been identified. Here we describe the endothelially derived secreted molecule Del-1 (developmental endothelial locus–1) as an anti-adhesive factor that interferes with the integrin LFA-1–dependent leukocyte-endothelial adhesion. Endothelial Del-1 deficiency increased LFA-1–dependent leukocyte adhesion in vitro and in vivo. Del-$1^{-/-}$ mice displayed significantly higher neutrophil accumulation in lipopolysaccharide-induced lung inflammation in vivo, which was reversed in Del-1/LFA-1 double-deficient mice. Thus, Del-1 is an endogenous inhibitor of inflammatory cell recruitment and could provide a basis for targeting leukocyte-endothelial interactions in disease.

Leukocyte extravasation is integral to the response to infection or injury and to inflammation and autoimmunity. Leukocyte recruitment comprises a well-coordinated cascade of adhesive events, including selectin-mediated rolling, firm adhesion of leukocytes to endothelial cells, and their subsequent transendothelial migration. The interaction between LFA-1 (also known as αLβ2 and CD11a/CD18) and endothelial intercellular adhesion molecule–1 (ICAM-1) is crucial during firm endothelial adhesion of leukocytes (*1–5*). Whereas numerous adhesion receptors promoting inflammatory cell recruitment have been identified, very little information exists about endogenous inhibitors of the leukocyte adhesion cascade (*1–7*).

Developmental endothelial locus–1 (Del-1) is a glycoprotein that is secreted by endothelial cells and can associate with the endothelial cell surface and the extracellular matrix (*8–10*). Del-1 is regulated upon hypoxia or vascular injury and has been implicated in vascular remodeling during angiogenesis (*10–12*). We sought to determine whether endothelially derived Del-1 participates in leukocyte-endothelial interactions.

Del-1 mRNA was observed predominantly in the brain and lung, with no expression in the liver, spleen, or whole blood (Fig. 1A and fig. S1A). Del-1 was expressed in wild-type (WT) but not in Del-$1^{-/-}$ murine lung endothelial cells (Fig. 1B) (*9*). In lung tissues, Del-1 was present in blood vessels (fig. S1B).

To determine whether Del-1 participates in leukocyte recruitment interactions, we studied the adhesion of primary neutrophils to immobi-

[1]Experimental Immunology Branch, Center for Cancer Research, National Cancer Institute (NCI), National Institutes of Health (NIH), Bethesda, MD, USA. [2]Molecular Cardiology, Department of Internal Medicine III, J. W. Goethe University, Frankfurt, Germany. [3]Department of Neurosurgery, Charite Universitätsmedizin, Berlin, Germany. [4]Institute for Molecular Cardiovascular Research, RWTH University Hospital, Aachen, Germany. [5]Laboratory of Cellular Oncology, Center for Cancer Research, NCI, NIH, Bethesda, MD, USA. [6]Division of Cardiovascular Medicine, Stanford University School of Medicine, Palo Alto, CA, USA. [7]Laboratory of Proteomics and Analytical Technologies, SAIC-Frederick, NCI, Frederick, MD, USA. [8]Baylor College of Medicine and Center for Cardiovascular Disease Prevention, Methodist DeBakey Heart and Vascular Center, Houston, TX, USA. [9]Department of Microbiology, Immunology and Tropical Medicine, George Washington University, Washington, DC, USA. [10]Molecular and Vascular Medicine, Beth Israel Deaconess Medical Center, Harvard Medical School, Boston, MA, USA. [11]Department of Medicine/Hematology, University of Washington, Seattle, WA, USA. [12]Division of Biochemistry, Faculty of Biosciences, University of Helsinki, Finland. [13]Dermatology Branch, Center for Cancer Research, NCI, NIH, Bethesda, MD, USA.

*These authors contributed equally to this work.
†These authors contributed equally to this work.
‡To whom correspondence should be addressed. E-mail: chavakist@mail.nih.gov

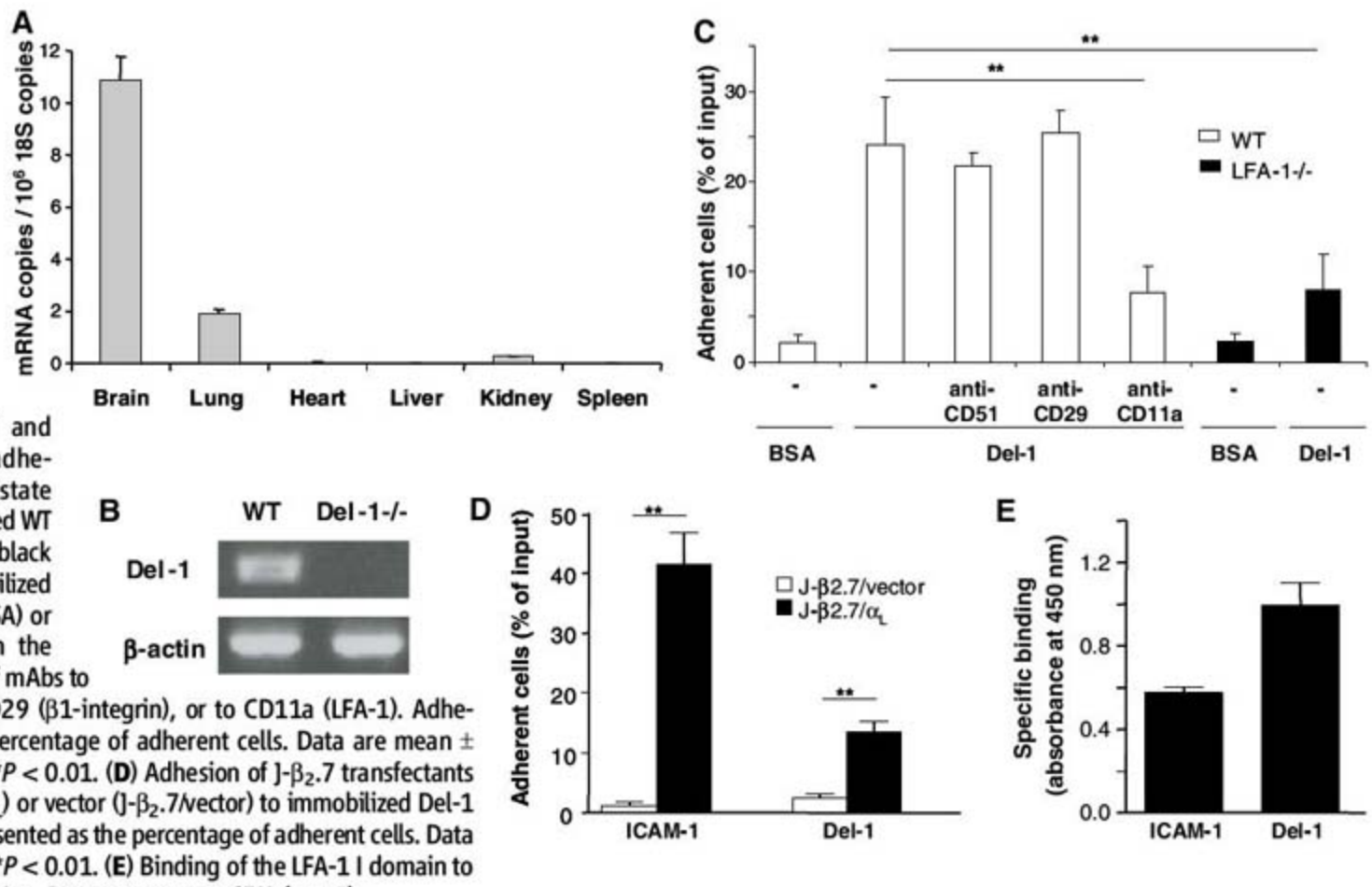

Fig. 1. Del-1 is expressed in endothelial cells and interacts with leukocyte LFA-1. (**A**) Real-time reverse transcription polymerase chain reaction (RT-PCR) demonstrating the expression of Del-1 mRNA in adult mouse tissues. Del-1 mRNA was normalized against 18*S* ribosomal RNA. (**B**) RT-PCR in primary lung endothelial cells from WT and Del-$1^{-/-}$ mice. (**C**) Static adhesion of phorbol 12-myristate 13-acetate (PMA)–stimulated WT (white bars) or LFA-$1^{-/-}$ (black bars) neutrophils to immobilized bovine serum albumin (BSA) or mouse Del-1 is shown in the absence (-) or presence of mAbs to CD51 (αv-integrin), to CD29 (β1-integrin), or to CD11a (LFA-1). Adhesion is presented as the percentage of adherent cells. Data are mean ± SD ($n = 3$ experiments). $^{**}P < 0.01$. (**D**) Adhesion of J-β_2.7 transfectants expressing LFA-1 (J-β_2.7/α_L) or vector (J-β_2.7/vector) to immobilized Del-1 or ICAM-1. Adhesion is presented as the percentage of adherent cells. Data are mean ± SEM ($n = 3$). $^{**}P < 0.01$. (**E**) Binding of the LFA-1 I domain to immobilized Del-1 or ICAM-1. Data are mean ± SEM ($n = 3$).

lized Del-1. Mouse neutrophils specifically bound to Del-1 under static conditions. Adhesion was inhibited by a blocking monoclonal antibody (mAb) to CD11a (the αL-integrin subunit) but not by antibodies to αv-integrin or β1-integrin (Fig. 1C), suggesting that LFA-1 mediates the interaction of neutrophils with Del-1. Consistently, LFA-$1^{-/-}$ neutrophils displayed reduced adhesion to Del-1 (Fig. 1C). The residual LFA-1–independent binding of neutrophils to Del-1 was blocked by mAb to Mac-1 (fig. S2A), which is consistent with the fact that LFA-1 and Mac-1 are closely related and share several ligands (*13*). In addition, αL-transfected but not vector-transfected J-β_2.7 cells specifically bound to immobilized Del-1 (Fig. 1D), whereas a direct interaction between Del-1 and the ligand-binding I domain of LFA-1, locked in the open high-affinity conformation, was observed (Fig. 1E and fig. S2B). Thus, Del-1 is a ligand of LFA-1 integrin.

To address whether Del-1 participates in leukocyte-endothelial interactions, we studied neutrophil and monocyte adhesion to WT and Del-$1^{-/-}$ endothelial cells (*14*, *15*). Contrary to our prediction, Del-$1^{-/-}$ endothelial cells promoted significantly higher neutrophil and monocyte adhesion. LFA-1–deficiency on leukocytes and mAb to LFA-1 abolished the enhanced adhesion to Del-$1^{-/-}$ endothelium (Fig. 2A and fig. S3). Thus, enhanced inflammatory cell adhesion to Del-$1^{-/-}$ endothelium is specifically mediated by LFA-1 on leukocytes.

To understand the unexpected inhibitory role of Del-1 in leukocyte-endothelial adhesion, we investigated whether soluble Del-1 interfered with the interaction of LFA-1 with its major ligand, ICAM-1. Mn^{2+}-induced binding of ICAM-1–Fc to murine leukocytes in solution was significantly inhibited by soluble Del-1 (Fig. 2B). Moreover, soluble Del-1 inhibited the LFA-1–dependent adhesion of WT neutrophils to immobilized ICAM-1 under physiologic flow conditions, whereas soluble Del-1 did not affect the weaker adhesion of LFA-$1^{-/-}$ neutrophils to ICAM-1 (Fig. 2C).

The finding that endothelial Del-1 antagonizes LFA-1–dependent adhesion (Fig. 2A) appeared to be discordant with the finding that immobilized Del-1 promoted leukocyte adhesion under static conditions (Fig. 1C). We thus assessed the ability of Del-1 and ICAM-1 to promote adhesion when co-immobilized with P-selectin and the chemokine MIP-2 under physiologic flow conditions at low and high shear rates (0.8 and 2 dynes/cm^2). In this system, leukocytes first roll on selectin and then arrest on the integrin ligand. Whereas ICAM-1 promoted robust firm adhesion of neutrophils at both shear rates, Del-1 promoted only weak adhesion at the lower shear rate and almost none at the higher shear rate (Fig. 2D). We then analyzed how the presence of plate-bound Del-1 would affect the adhesion of neutrophils to ICAM-1 under flow. Increasing concentrations of Del-1 co-immobilized with ICAM-1, P-selectin, and MIP-2 significantly inhibited neutrophil adhesion to ICAM-1 (Fig. 2E). Thus, although it is

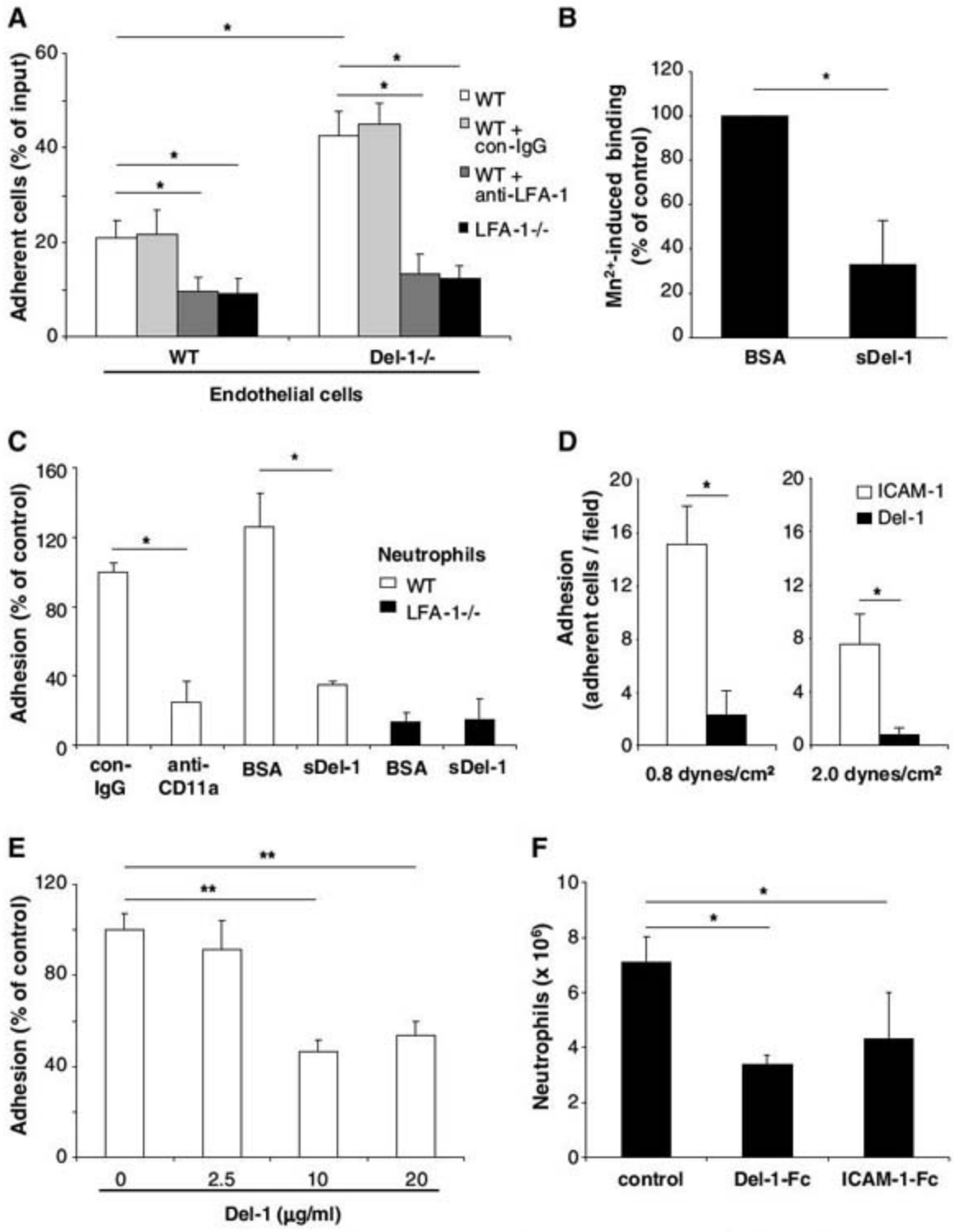

Fig. 2. Del-1 interferes with LFA-1–dependent leukocyte adhesion. (**A**) PMA-induced adhesion of WT neutrophils in the absence (white bars) or presence of isotype control antibody (light gray bars) or mAb to LFA-1 (dark gray bars), or of LFA-$1^{-/-}$ neutrophils (black bars) to WT or Del-$1^{-/-}$ lung endothelial cells, is shown. IgG, immunogolbulin G. Adhesion is presented as the percentage of adherent cells. Data are mean ± SD (n = 4 experiments). *P < 0.05. (**B**) Binding of soluble ICAM-1–Fc to mouse bone marrow mononuclear cells in the presence of $MnCl_2$. Cells were preincubated with BSA or soluble Del-1. Data are mean ± SEM (n = 3). *P < 0.05. (**C**) Adhesion of WT (white bars) or LFA-$1^{-/-}$ (black bars) neutrophils to immobilized P-selectin, MIP-2, and ICAM-1 under flow (0.8 dynes/cm^2) was studied in the presence of mAb to CD11a or isotype control antibody (each mAb at 10 μg/ml) or in the presence of BSA or mouse soluble Del-1 (each at 20 μg/ml). Adhesion is shown as the percentage of control; that is, adhesion of WT neutrophils in the presence of control antibody. Data are mean ± SEM (n = 3 perfusion experiments). *P < 0.05. (**D**) Adhesion of WT neutrophils to immobilized P-selectin, MIP-2, and ICAM-1 (white bars) or Del-1 (black bars) was studied at indicated shear rates. Adhesion is shown as the number of adherent cells per field. Data are mean ± SEM (n = 4 perfusion experiments). *P < 0.05. (**E**) Adhesion of WT neutrophils to immobilized P-selectin, MIP-2, and ICAM-1 was studied in the presence of increasing concentrations of Del-1 that was coimmobilized. Adhesion is shown as the percentage of control; that is, adhesion of WT neutrophils in the absence of immobilized Del-1. Data are mean ± SEM (n = 6 perfusion experiments). **P < 0.01. (**F**) The numbers of neutrophils at 4 hours after intraperitoneal injection of thioglycollate in WT mice are shown. Mice were treated 30 min before thioglycollate injection with intravenous injection of control Fc protein (control), Del-1–Fc, or ICAM-1–Fc. Data are expressed as absolute numbers of emigrated neutrophils. Data are mean ± SD (n = 4 mice per group). *P < 0.05.

a ligand of LFA-1, Del-1 does not promote firm leukocyte adhesion under flow but interferes with leukocyte adhesion to endothelial ICAM-1.

We then assessed the ability of soluble Del-1 expressed as an Fc fusion protein to inhibit neutrophil recruitment in vivo in acute thioglycollate-induced peritonitis (*14*). Intravenous administration of Del-1–Fc 30 min before thioglycollate injection significantly reduced neutrophil accumulation,

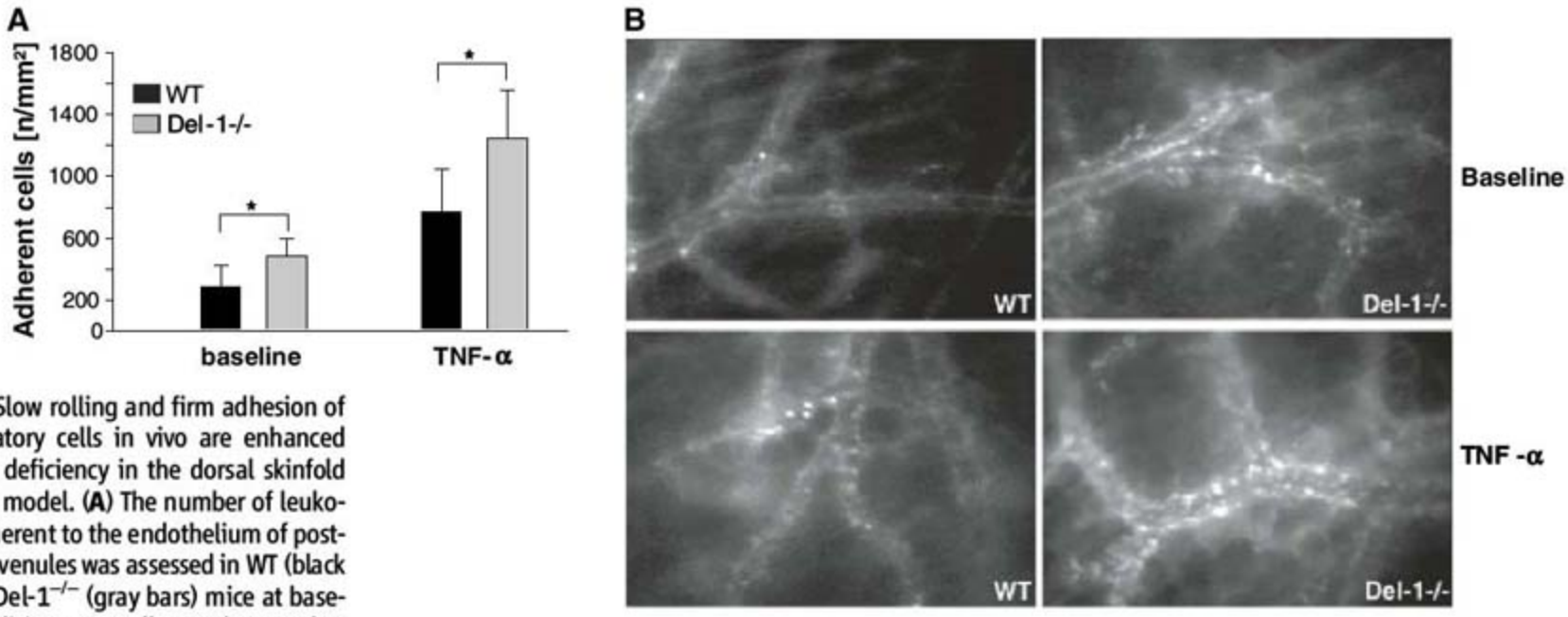

Fig. 3. Slow rolling and firm adhesion of inflammatory cells in vivo are enhanced by Del-1 deficiency in the dorsal skinfold chamber model. (**A**) The number of leukocytes adherent to the endothelium of postcapillary venules was assessed in WT (black bars) or Del-$1^{-/-}$ (gray bars) mice at baseline conditions as well as 2 hours after TNF-α superfusion. Adherent leukocytes are shown as the number of cells per vessel surface (in square millimeters). Data are mean ± SD (n = 5 mice per group). *P < 0.05. (**B**) Representative images of rhodamine 6G–labeled leukocytes adherent onto the endothelium of postcapillary venules of WT and Del-$1^{-/-}$ mice. (**C**) The average rolling leukocyte velocities at 2 hours after TNF-α superfusion in WT (black bar) and Del-$1^{-/-}$ (gray bar) mice are shown. Data are mean ± SD (n = 5 mice per group). **P < 0.01. (**D**) The rolling flux fraction at 2 hours after TNF-α superfusion in WT (black circles) and Del-$1^{-/-}$ (gray squares) mice.

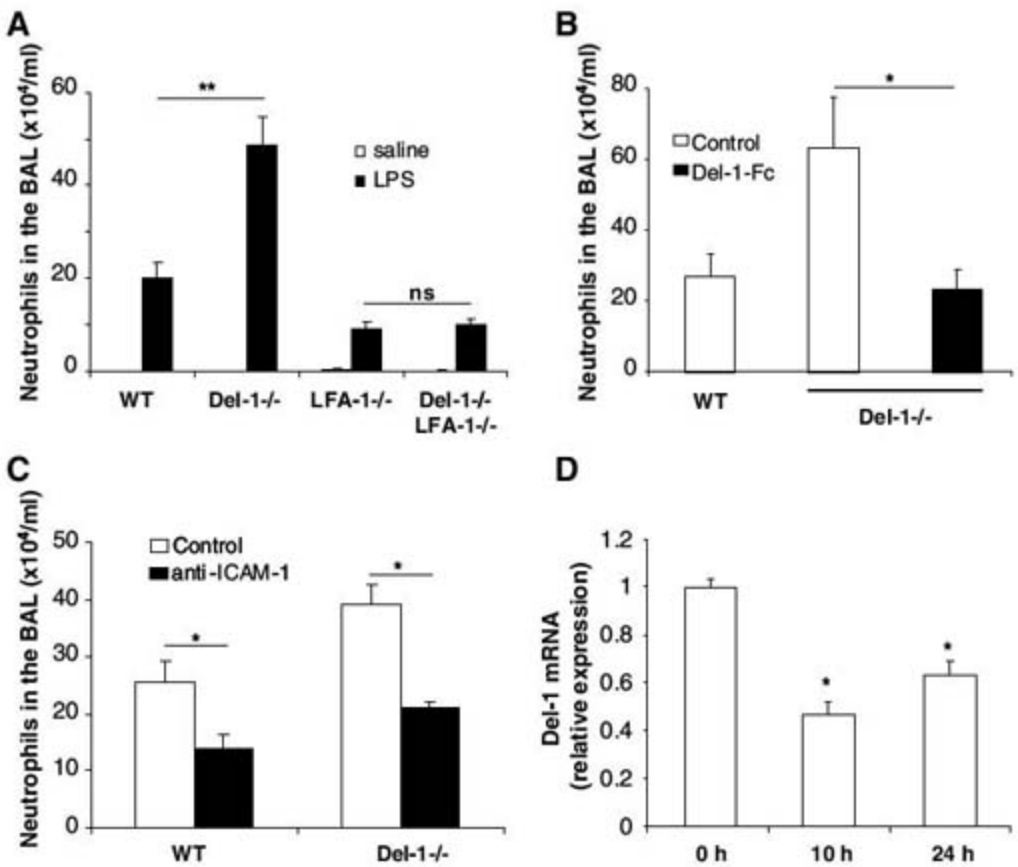

Fig. 4. Increased inflammatory cell recruitment in vivo due to Del-1 deficiency. (**A**) The numbers of neutrophils in the BAL fluid in WT, Del-$1^{-/-}$, LFA-$1^{-/-}$, or Del-$1^{-/-}$LFA-$1^{-/-}$ mice are shown at 24 hours after nasal administration of saline (white bars) or LPS (black bars). Neutrophil recruitment upon saline inhalation was negligible. Data are expressed as absolute numbers and are mean ± SEM (n = 11 to 16 mice per group). **P < 0.01; ns, not significant. (**B**) Thirty minutes before LPS administration, WT or Del-$1^{-/-}$– mice received intravenous injections of BSA (control, white bars) or Del-1-Fc (black bar) (each at 90 μg per mouse). Data are expressed as absolute numbers and are mean ± SEM (n = 4 to 11 mice per group). *P < 0.05. (**C**) Thirty minutes before LPS administration, WT or Del-$1^{-/-}$ mice received intravenous injections of isotype control IgG (white bars) or anti-ICAM-1 (black bars) (each at 85 μg per mouse). Data are expressed as absolute numbers and are mean ± SEM (n = 8 or 9 mice per group). *P < 0.05. (**D**) The expression of Del-1 mRNA in mouse lungs at 0 hours, 10 hours, or 24 hours after intranasal LPS administration was analyzed by semiquantitative RT-PCR. The data are shown as relative expression. The ratio of Del-1 mRNA to actin mRNA at 0 hours was set as 1. Data are mean ± SEM (n = 4 mice per group). *P < 0.05 as compared to 0 hours.

as compared to Fc control protein (Fig. 2F). Similarly, ICAM-1–Fc reduced neutrophil recruitment into the peritoneum (Fig. 2F).

To provide further evidence for the role of Del-1 in inflammatory cell recruitment in vivo, we performed intravital microscopy using the dorsal skinfold chamber model (*16*). Del-1$^{-/-}$ mice displayed increased numbers of leukocytes adherent to postcapillary venules both in the baseline condition and upon tumor necrosis factor–α (TNF-α) stimulation (Fig. 3, A and B). Besides firm arrest, the interaction between LFA-1 and ICAM-1 contributes to slow rolling processes (*17*). A significant decrease in rolling velocity accompanied by an increase in the fraction of slow-rolling leukocytes was observed in Del-1$^{-/-}$ mice (Fig. 3, C and D).

We further studied whether Del-1 could regulate inflammatory cell recruitment in vivo, by performing LPS-induced lung inflammation. Del-1$^{-/-}$ mice displayed significantly higher accumulation of neutrophils in the bronchoalveolar lavage (BAL) fluid than did WT mice (Fig. 4A). LFA-1$^{-/-}$ mice displayed reduced neutrophil accumulation in the BAL upon LPS-induced lung inflammation (Fig. 4A) (*18*, *19*). The increased neutrophil recruitment in vivo due to Del-1 deficiency required the presence of LFA-1, because neutrophil accumulation in the BAL in Del-1$^{-/-}$LFA-1$^{-/-}$ mice equaled the accumulation of these cells in LFA-1$^{-/-}$ mice (Fig. 4A). The increased leukocyte recruitment due to Del-1 deficiency could not be attributed to an alteration in peripheral blood counts, because constitutive leukocyte numbers were comparable in WT and Del-1$^{-/-}$ mice (fig. S4). In addition, intravenous administration of soluble Del-1 efficiently reversed the increased neutrophil recruitment in Del-1$^{-/-}$ mice (Fig. 4B).

Furthermore, Del-1 deficiency resulted in an up-regulation of baseline ICAM-1 protein expression by lung endothelial cells, which was overridden upon TNF-α stimulation, whereas vascular cell adhesion molecule–1 (VCAM-1) expression was unaffected (fig. S5). No significant increase in ICAM-1 expression, under baseline or inflammatory conditions, was found in Del-1$^{-/-}$ lungs (fig. S6), suggesting that altered ICAM-1 expression is not involved in the increased leukocyte recruitment to Del-1$^{-/-}$ lungs. Moreover, whereas the increased neutrophil recruitment to the lung upon Del-1 deficiency was completely reversed by leukocyte LFA-1 deficiency (Fig. 4A), the inhibition of ICAM-1 by a blocking mAb (*18*, *20*) decreased neutrophil recruitment by the same extent in both WT and Del-1$^{-/-}$ mice (Fig. 4C), suggesting an involvement of other LFA-1 ligands. Thus, Del-1 deficiency enhances LFA-1–dependent leukocyte recruitment in vivo.

We found that Del-1 acted in an anti-inflammatory fashion; however, the expression of Del-1 in inflammation has not been demonstrated. Thus, we analyzed Del-1 mRNA expression in the lung and in endothelial cells upon inflammatory stimulation. Upon LPS administration, lung Del-1 mRNA was significantly reduced (Fig. 4D). Likewise, TNF-α stimulation of endothelial cells induced a significant decrease in Del-1 expression (fig. S7).

Endogenous inhibitors exist in many aspects of inflammation and immunity (*21*, *22*), attenuating exuberant inflammatory and immune activation. The existence of endogenous inhibitors in the leukocyte adhesion cascade, a central paradigm of inflammation and immunity, has been unclear. In this study, endothelially derived Del-1 was shown to intercept LFA-1–dependent leukocyte-endothelial interactions. Given the importance of LFA-1–dependent leukocyte recruitment in several inflammatory and autoimmune disorders (*13*, *23*–*25*), Del-1 may provide a platform for designing novel attractive therapeutic modalities to target leukocyte-endothelial interactions in disease.

References and Notes

1. T. A. Springer, *Cell* **76**, 301 (1994).
2. N. Hogg, M. Laschinger, K. Giles, A. McDowall, *J. Cell Sci.* **116**, 4695 (2003).
3. D. Vestweber, *Immunol. Rev.* **218**, 178 (2007).
4. B. A. Imhof, M. Aurrand-Lions, *Nat. Rev. Immunol.* **4**, 432 (2004).
5. K. Ley, C. Laudanna, M. I. Cybulsky, S. Nourshargh, *Nat. Rev. Immunol.* **7**, 678 (2007).
6. C. Weber, L. Fraemohs, E. Dejana, *Nat. Rev. Immunol.* **7**, 467 (2007).
7. T. Chavakis, K. T. Preissner, M. Herrmann, *Trends Immunol.* **28**, 408 (2007).
8. C. Hidai, M. Kawana, H. Kitano, S. Kokubun, *Cell Tissue Res.* **330**, 83 (2007).
9. C. Hidai *et al.*, *Genes Dev.* **12**, 21 (1998).
10. H. K. Ho *et al.*, *Circulation* **109**, 1314 (2004).
11. K. Penta *et al.*, *J. Biol. Chem.* **274**, 11101 (1999).
12. J. Zhong *et al.*, *J. Clin. Invest.* **112**, 30 (2003).
13. C. G. Gahmberg *et al.*, *Cell. Mol. Life Sci.* **54**, 549 (1998).
14. Materials and methods are available as supporting material on *Science* Online.
15. E. Y. Choi *et al.*, *Blood* **111**, 3607 (2008).
16. U. Fiedler *et al.*, *Nat. Med.* **12**, 235 (2006).
17. A. Zarbock, C. A. Lowell, K. Ley, *Immunity* **26**, 773 (2007).
18. A. Basit *et al.*, *Am. J. Physiol. Lung Cell. Mol. Physiol.* **291**, L200 (2006).
19. Z. M. Ding *et al.*, *J. Immunol.* **163**, 5029 (1999).
20. T. Kumasaka *et al.*, *J. Clin. Invest.* **97**, 2362 (1996).
21. R. V. Parry, J. L. Riley, S. G. Ward, *Trends Immunol.* **28**, 161 (2007).
22. R. J. Greenwald, G. J. Freeman, A. H. Sharpe, *Annu. Rev. Immunol.* **23**, 515 (2005).
23. M. Lebwohl *et al.*, *New Engl. J. Med.* **349**, 2004 (2003).
24. A. D. Luster, R. Alon, U. H. von Andrian, *Nat. Immunol.* **6**, 1182 (2005).
25. K. Yonekawa, J. M. Harlan, *J. Leukoc. Biol.* **77**, 129 (2005).

26. We thank X. Feng and M. Sardy for generating the Del-1–Fc protein, N. Hogg for the antibody mAb24, Valentis Inc. for recombinant Del-1 and the antibody to mouse Del-1, T. Veenstra for help with mass spectrometry, D. Winkler for help with genotyping, I. Okwumabua for technical assistance, and D. Singer for critically reading the manuscript. This research was supported by the Intramural Research Program of the NIH, NCI (T.C. and M.C.U.); by NIH grants AI067254 (S.L.C.) and RO1 HL082927 (W.C.A.); and by the Deutsche Forschungsgemeinschaft (grants FOR809 and TP6 to C.W.; TR-SFB23 and Exc 147/1 to S.D. and E.C.). A patent application on the anti-inflammatory actions of Del-1 has been filed.

Supporting Online Material

www.sciencemag.org/cgi/content/full/322/5904/1101/DC1
Materials and Methods
Figs. S1 to S8
References

28 August 2008; accepted 9 October 2008
10.1126/science.1165218

Ubiquitin-Like Protein Involved in the Proteasome Pathway of *Mycobacterium tuberculosis*

Michael J. Pearce,[1] Julian Mintseris,[2] Jessica Ferreyra,[1] Steven P. Gygi,[2] K. Heran Darwin[1]*

The protein modifier ubiquitin is a signal for proteasome-mediated degradation in eukaryotes. Proteasome-bearing prokaryotes have been thought to degrade proteins via a ubiquitin-independent pathway. We have identified a prokaryotic ubiquitin-like protein, Pup (Rv2111c), which was specifically conjugated to proteasome substrates in the pathogen *Mycobacterium tuberculosis*. Pupylation occurred on lysines and required proteasome accessory factor A (PafA). In a *pafA* mutant, pupylated proteins were absent and substrates accumulated, thereby connecting pupylation with degradation. Although analogous to ubiquitylation, pupylation appears to proceed by a different chemistry. Thus, like eukaryotes, bacteria may use a small-protein modifier to control protein stability.

Similar to the eukaryotic 20*S* proteasome, the *Mycobacterium tuberculosis* (*Mtb*) proteasome is a multisubunit barrel-shaped protease composed of two rings of catalytic β subunits sandwiched by rings of α subunits (*1*–*5*). The eukaryotic 26*S* proteasome is composed of a 20*S* core particle and one or two 19*S* regulatory caps, which include adenosine triphosphatases (ATPases) that recognize, unfold, and translocate substrates into the core for degradation [reviewed in (*6*)]. In *Mtb*, Mpa (*Mycobacterium* proteasome ATPase) shares homology with regulatory cap ATPases. Substrates of the *Mtb* proteasome have been identified (*7*), but it remains unclear how they were targeted for degradation. Proteins delivered to the eukaryotic proteasome are usually conjugated with

ubiquitin, which covalently attaches to substrate lysines (Lys) as well as onto ubiquitin itself [reviewed in (*8*)]. Genes encoding ubiquitin-like proteins (Ubls) have not been identified in the *Mtb* genome.

To further define the *Mtb* proteasome system, we looked for proteins that interacted with Mpa using an *Escherichia coli* bacterial two-hybrid system (*9*, *10*). A fusion protein that encoded the last 26 amino acids of Rv2111c (here referred to as "Pup") interacted with the Mpa bait fusion [Fig. 1A (*10*)]. Full-length Pup also specifically interacted with Mpa (Fig. 1A). The *pup* gene has been identified (*11*, *12*), but the function of Pup was unknown. *pup* homologs have so far only been identified in Actinobacteria by BLAST search (*13*). In *Mtb*, *pup* is part of a putative operon with the proteasome core genes *prcB* and *prcA* (fig. S2). *pup* is predicted to encode a 64–amino acid protein with a molecular size of 6.9 kD (GenBank accession number EU914921). Recombinant Pup purified from *E. coli* migrated to a position around 15 kD in a denaturing polyacrylamide gel (Fig. 1B); however, certain Ubls, like SUMO-1, migrate more slowly than expected (*14*, *15*).

We then tested the Pup/Mpa interaction in vitro using nickel-nitrilotriacetic acid (Ni-NTA) agarose bound with purified His_6-Pup, and Pup was able to bind Mpa (Fig. 1B) (*10*). Mpa was not retained by agarose that had first been incubated with *E. coli* lysate or with SigE-His_6, a *Salmonella typhimurium* protein that is similar in size and charge to Pup (*16*). Thus, Pup specifically and noncovalently interacted with Mpa in an *E. coli* lysate under native conditions.

Additional genetic and biochemical experiments with *E. coli* to test for interactions between Pup and other *Mtb* proteasome components were unsuccessful. Thus, we hypothesized that *E. coli* lacked cofactors that were necessary to promote certain *Mtb* protein-protein interactions. We therefore used a mycobacterial protein fragment complementation assay (*17*) to test for interactions between various *Mtb* proteasome components and substrates in *Mycobacterium smegmatis* (*Msm*). Surprisingly, we observed a strong positive interaction between Pup and the proteasome substrate FabD [malonyl coenzyme A acyl carrier protein] (Fig. 1C). To confirm the interaction, we expressed constructs encoding FLAG-FabD and His_6-Pup in *Msm*. Antibodies to FLAG (anti-FLAG) detected purified FLAG-FabD at the predicted size of ~30 kD (Fig. 1D). Unexpectedly, His_5-specific antibodies detected a purified ~45-kD species when FLAG-FabD and His_6-Pup were coproduced in mycobacteria (Fig. 1D). We also observed the ~45-kD band upon a longer exposure with anti-FLAG (fig. S3A). This ~45-kD species, probably representing a Pup~FabD complex, was highly stable because it was maintained under reducing and denaturing conditions. When FLAG-FabD was purified from an *E. coli* strain making His_6-Pup, we were unable to detect the ~45-kD species (fig. S3B). Thus, Pup interacts with an *Mtb* proteasome substrate in a manner that is not supported in *E. coli*, and requires *Mycobacterium*-specific factors.

The formation of a stable complex between our model substrate FabD and Pup was reminiscent of the covalent attachment of ubiquitin to proteasome substrates in eukaryotes. Sequence and structural prediction comparisons between Pup and ubiquitin showed no overall homology. However, we noticed conservation of either of the basic amino acids arginine (Arg) or Lys, followed by two glycines (Gly) at the C termini (Fig. 2A). This di-Gly motif is conserved in most members of the ubiquitin-like protein family, and is usually followed by one or more amino acids [reviewed in (*18*)]. The C termini of Ubls are generally processed to expose the di-Gly and

[1]Department of Microbiology, New York University School of Medicine, New York, NY 10016, USA. [2]Department of Cell Biology, Harvard Medical School, Boston, MA 02115, USA.

*To whom correspondence should be addressed. E-mail: heran.darwin@med.nyu.edu

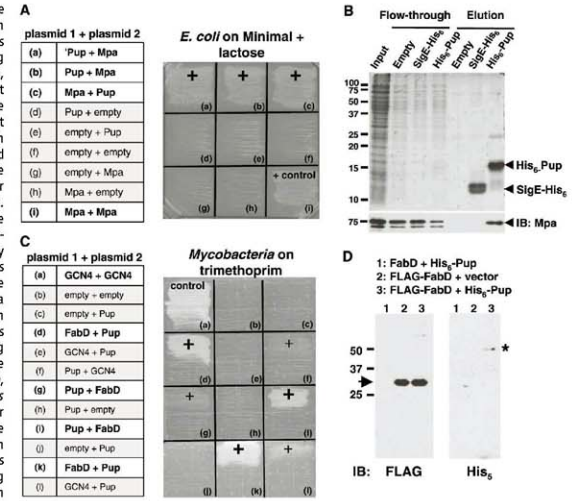

Fig. 1. Pup interacts with the ATPase Mpa and the proteasome substrate FabD. **(A)** Mpa interacted with Pup in an *E. coli* two-hybrid system. *E. coli* (*cya*) was transformed with combinations of plasmids encoding either of the two domains of *Bordetella pertussis* Cya, T25 ("plasmid 1") or T18 ("plasmid 2"), fused to test proteins (for plasmid details, see fig. S1A and table S1). 'Pup represents the 26–amino acid fragment identified from an *Mtb* genomic T25 library with T18C-Mpa as bait (a). Interactions that reconstituted functional Cya permitted growth on minimal lactose agar ("+"). All strains grew on minimal glucose agar (fig. S1A). **(B)** Mpa interacted with Pup in vitro. His_6-Pup, SigE-His_6, or *E. coli* "vector only" lysate on Ni-NTA agarose was incubated with recombinant Mpa ("input"). Fractions were separated by 15% SDS–polyacrylamide gel electrophoresis (PAGE) and visualized with Coomassie Brilliant Blue (CBB). The same samples were analyzed by anti-Mpa immunoblot (IB, below). **(C)** Pup interacted with FabD in an *Msm* two-hybrid system. *Msm* was transformed with combinations of plasmids encoding either of the two domains of murine dihydrofolate reductase, F(1,2) ("plasmid 1") or F(3) ("plasmid 2"), fused to Pup, FabD, GCN4 (a *Saccharomyces cerevisiae* leucine zipper domain), or no other protein (for plasmid details, see fig. S1B and table S1). Positive interactions permitted growth on trimethoprim (Trim) ("+"). Pup had weak interactions with GCN4 (f, l). All strains grew on media lacking Trim (fig. S1B). **(D)** Pup formed a stable complex with FabD in *Msm*. FLAG-tagged proteins were enriched from equal amounts of lysates of *Msm* with plasmids encoding FLAG-FabD and either empty vector or His_6-Pup. Untagged FabD was the negative control. Samples were separated by 12% SDS-PAGE, and analyzed by anti-FLAG or anti-His_5 immunoblotting. FLAG-FabD migrated at the predicted size (arrow, left) and at a higher molecular size (fig. S3A); the ~45-kD anti-His_5–reactive protein (asterisk, right) is only seen in mycobacteria producing FLAG-FabD and His_6-Pup.

then activated for conjugation to substrate proteins through a series of enzyme-catalyzed reactions [reviewed in (*19*)]. The terminal Gly of ubiquitin is essential for the formation of an isopeptide bond with the Lys of a substrate [reviewed in (*8*)].

Consequently, we used tandem affinity chromatography to purify FLAG-FabD~His_6-Pup (Fig. 2B) and characterized the interaction using mass spectrometry (MS) (*20*). MS analysis of ubiquitylated substrates typically identifies substrate peptides with the tryptic Gly-Gly ubiquitin fragment covalently attached to a lysine (*20*). Our MS analysis confirmed the presence of both *Mtb* proteins and, given the Pup C-terminal sequence (Gly-Gly-Gln; Gln, glutamine), we performed a high-resolution tandem MS/MS search allowing for either a Gly-Gly or Gly-Gly-Gln modification of FabD (Fig. 2C). This analysis revealed several spectral matches to a FabD tryptic peptide with the Pup C-terminal sequence attached through an isopeptide bond to Lys^{173} of FabD. The precursor mass deviation (ΔM), however, suggested a deamidation event ($\Delta M = +0.984$), pointing to a probable C-terminal Gln→Glu conversion. This result showed that the Gln following the di-Gly of Pup was not removed. We then purified unconjugated His_6-Pup from *E. coli* and *Msm*, digested the protein with Asp-N protease, and analyzed peptides by MS/MS. Using the raw intensity data, we estimated roughly a 1:10 ratio of deamidated Gln:Gln at the Pup C terminus when purified from *E. coli* (Fig. 2D). In contrast, the deamidated form dominated by two orders of magnitude in *Msm*, strongly suggesting that enzymatic activity was responsible for the conversion of Pup into its active form. Thus, deamidated Pup was covalently bound to a specific Lys residue of an *Mtb* proteasome substrate in a manner analogous to the conjugation of ubiquitin to eukaryotic proteasome substrates.

FabD and other *Mtb* proteasome substrates accumulate in *mpa* and *pafA* mutants (*7*). If Pup, like ubiquitin, targets proteins for degradation, pupylated FabD should also accumulate in these mutants. FLAG-tagged FabD abundance was increased in the *mpa* and *pafA* strains compared to wild-type (WT) *Mtb* (Fig. 3A). We detected Pup~FabD in WT *Mtb*, and an accumulation of this species in the *mpa* mutant (Fig. 3A). We also observed Pup~FabD in WT samples using FLAG-specific antibodies (Fig. 3A). Pup~FabD is present at extremely low steady-state amounts, suggesting that the transition from an unpupylated to a pupylated state is a tightly regulated process, like that of Ubl conjugation (*19*, *21*). Unexpectedly, Pup~FabD was undetectable in the *pafA* strain (Fig. 3A), despite the accumulation of unpupylated FabD. Similar observations were made for another *Mtb* proteasome substrate, PanB (ketopantoate hydroxymethyltransferase) (fig. S6A), but not for DlaT (dihydrolipoamide acyltransferase) (Fig. 3A), which is not a substrate (*7*). Therefore, PafA is involved in pupylation, a process that seems to be specific for *Mtb* proteasome substrates.

If Pup acts like ubiquitin, then multiple pupylated proteins could exist in *Mtb*. Immunoblot analysis with a Pup-specific antibody against soluble proteins from WT and *mpa Mtb* strains revealed a ladder of proteins (Fig. 3B). Again, no anti-Pup reactive bands were observed in the *pafA* sample (Fig. 3B), implying that this phenomenon extends to all targets of pupylation within the limits of detection. We were unable to detect the unconjugated form of Pup, suggesting that most Pup molecules are conjugated to substrates at steady state, or are rapidly degraded by an unidentified protease. Because *pafA* is in an operon with *pafBC*, we also tested *pafB* and *pafC* mutants for substrate pupylation (Fig. 3B). The extent of pupylation did not differ between the WT strain and the *pafBC* mutants, confirming that PafB and PafC do not seem to be involved in substrate degradation (*22*).

Our data suggest that PafA-dependent pupylation of Lys^{173} leads to the degradation of FabD. To test this hypothesis, we followed the stability of purified ^{35}S-labeled FLAG-FabD-

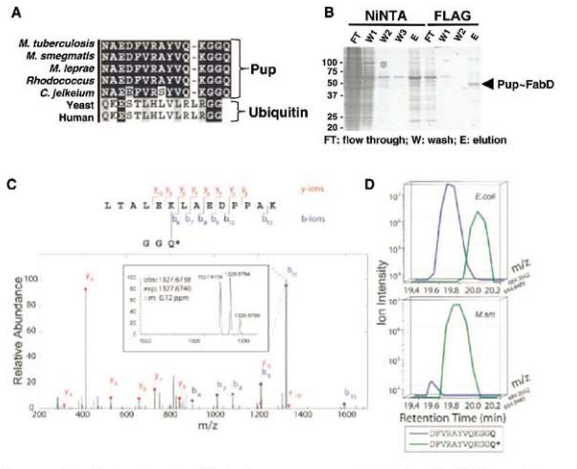

Fig. 2. The C terminus of *Mtb* Pup covalently attaches to Lys^{173} of *Mtb* FabD. **(A)** Alignment of the C terminus of Pup to that of Pup or ubiquitin from representative Actinomycetes or eukaryotes, respectively. Identical amino acids are shaded black. Sequences were compiled from the National Center for Biotechnology Information server and aligned by means of ClustalW (*23*). **(B)** Purification of the FabD~Pup complex. *Msm* was cotransformed with plasmids encoding FLAG-FabD and His_6-Pup. FLAG-FabD~His_6-Pup was purified sequentially with Ni-NTA agarose and anti-FLAG M2 affinity matrix. Proteins from each purification step were analyzed by 12% SDS-PAGE and visualized with CBB. **(C)** Tandem mass (MS/MS) spectrum of a FabD tryptic peptide derived by collision-induced dissociation of the $(M + 2H)^{2+}$ precursor, mass/charge ratio (m/z) 869.963 [1.55 parts per million (ppm)]. Singly charged fragment ions marked in the spectrum represent peptide bond cleavage resulting in the sequence information recorded from both the N and C termini (b- and y-type ions, respectively). This spectrum, searched with the SEQUEST program, matched to the peptide shown with a mass shift corresponding to a deamidation event, converting the Pup C-terminal Gln to Glu (Q*). High mass accuracy MS/MS unambiguously confirms covalent modification of lysine in FLAG-FabD by His_6-Pup, with multiple matching b- and y-type ions. Additional detailed fragment ion information and additional spectra are presented in fig. S4. **(D)** Extracted ion chromatograms of the C-terminal peptide of Asp-N–digested His_6-Pup. The traces correspond to the m/z of MH_3^{2+} precursors ±3 ppm). In *E. coli*, deamidated Gln was detected at a low abundance (~10%), whereas in *Msm*, the C-terminal Gln deamidation predominated. Q* denotes a deamidated Gln, equivalent to Glu. See fig. S5 and (*10*) for additional details. Amino acid residues: A, Ala; D, Asp; E, Glu; F, Phe; G, Gly; H, His; K, Lys; L, Leu; N, Asn; P, Pro; Q, Gln; R, Arg; S, Ser; T, Thr; V, Val; and Y, Tyr.

K173A-His_6 from WT *Msm*. The K173A mutant was markedly more stable than WT FabD (Fig. 4, A and B), providing further evidence that pupylation is a signal for degradation. We then purified radiolabeled His_6-pupylated proteins from WT and *mpa*-deficient *Msm* and observed the disappearance of these proteins over time in WT but not *mpa*-deficient bacteria (Fig. 4C and fig. S7). Thus, Pup covalently conjugates to a specific Lys of an *Mtb* proteasome substrate, and pupylated proteins are degraded in an Mpa/proteasome-dependent manner (fig. S8).

There are similarities between the ubiquitin and Pup systems, but there are also notable differences. Unique aspects of pupylation may include the mechanism of Pup activation and conjugation to substrates, the chemistry involved in the linkage of Pup to Lys, and the involvement of PafA. We speculate that PafA plays a part in conjugating Pup to substrates, but this idea requires further investigation. Additionally, it remains to be determined if proteins can be polypupylated in *Mtb*.

Aside from a role in protein degradation, Pup and other small protein modifiers may have important implications for other cellular processes in bacteria. Considering the multitude of activities coordinated by ubiquitylation or SUMOylation in eukaryotes (*19*, *21*), prokaryotes may also use posttranslational protein modifiers for functions ranging from subcellular sorting to secretion.

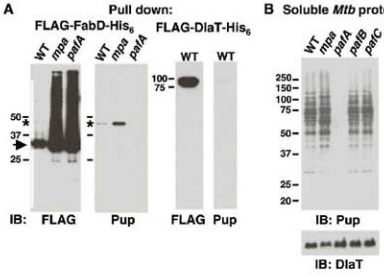

Fig. 3. Pupylation is associated with *Mtb* proteasome substrates. **(A)** Aberrant amounts of pupylation correlated with proteasome-defective states. Equal amounts of soluble *Mtb* lysates from WT, *mpa* and *pafA* strains were incubated with Ni-NTA agarose for enrichment of FLAG-FabD-His_6. Samples were deliberately overloaded to detect pupylated protein and observe the relative amounts of unpupylated versus pupylated FabD. Anti-FLAG immunoblots of Ni-NTA eluates detected both unpupylated (arrow) and pupylated (asterisk) FLAG-FabD-His_6. Anti-Pup immunoblots of the same samples detected Pup–FLAG-FabD-His_6 (asterisk) in WT and *mpa* *Mtb* but not in the *pafA* strain. As a control, FLAG-DlaT-His_6 was purified from WT *Mtb*. Anti-FLAG immunoblots detected a protein at the predicted size of FLAG-DlaT-His_6, but no pupylated species was detected. Ponceau S staining shows that protein is present on this membrane (fig. S6B). **(B)** Multiple pupylated proteins were present in *Mtb*, but not in a *pafA* mutant. Anti-Pup immunoblots of *Mtb* lysates from WT, *mpa*, *pafA*, *pafB*, and *pafC* strains. Equivalent cell numbers were analyzed and the same blot was used for detection of endogenous DlaT. All samples were separated by 10% SDS-PAGE.

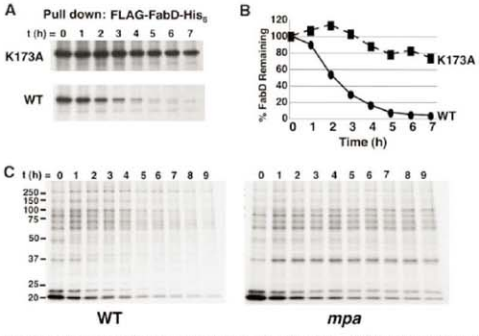

Fig. 4. Pupylation is required for Mpa-dependent protein degradation. **(A)** K173A mutation stabilized FabD. WT *Msm* expressing WT *fabD* or *fabD* with the K173 codon mutated to alanine was pulse labeled with ^{35}S-methionine and cysteine. Samples were collected over time and FLAG-FabD-His_6 (WT or K173A mutant) was purified and analyzed by 10% SDS-PAGE (*10*). This image represents a 12-hour exposure. A 6-hour exposure of the same gel is shown in fig. S7A. Immunoblot analysis showed that the K173A mutant was also not efficiently pupylated (fig. S7B). **(B)** Quantification of labeled protein in (A). **(C)** Pupylated proteins were degraded in an Mpa-dependent manner. WT and *mpa* mutant *Msm* were treated as in (A) and His_6-pupylated proteins were purified and analyzed. Total ^{35}S protein labeling is shown in fig. S7C. All data are representative of at least two independent experiments.

References and Notes

1. N. Benaroudj, P. Zwickl, E. Seemuller, W. Baumeister, A. L. Goldberg, *Mol. Cell* **11**, 69 (2003).
2. M. Groll *et al.*, *Nature* **386**, 463 (1997).
3. G. Hu *et al.*, *Mol. Microbiol.* **59**, 1417 (2006).
4. G. Lin *et al.*, *Mol. Microbiol.* **59**, 1405 (2006).
5. M. Unno *et al.*, *Structure* **10**, 609 (2002).
6. W. Baumeister, J. Walz, F. Zühl, E. Seemüller, *Cell* **92**, 367 (1998).
7. M. J. Pearce *et al.*, *EMBO J.* **25**, 5423 (2006).
8. A. Hershko, A. Ciechanover, *Annu. Rev. Biochem.* **67**, 425 (1998).
9. G. Karimova, J. Pidoux, A. Ullmann, D. Ladant, *Proc. Natl. Acad. Sci. U.S.A.* **95**, 5752 (1998).
10. Materials and methods are available as supporting material on *Science* Online.
11. N. Knipfer, T. E. Shrader, *Mol. Microbiol.* **25**, 375 (1997).
12. T. Tamura *et al.*, *Curr. Biol.* **5**, 766 (1995).
13. S. F. Altschul *et al.*, *Nucleic Acids Res.* **25**, 3389 (1997).
14. R. Mahajan, C. Delphin, T. Guan, L. Gerace, F. Melchior, *Cell* **88**, 97 (1997).
15. M. J. Matunis, E. Coutavas, G. Blobel, *J. Cell Biol.* **135**, 1457 (1996).
16. K. H. Darwin, L. S. Robinson, V. L. Miller, *J. Bacteriol.* **183**, 1452 (2001).
17. A. Singh, D. Mai, A. Kumar, A. J. Steyn, *Proc. Natl. Acad. Sci. U.S.A.* **103**, 11346 (2006).
18. M. Hochstrasser, *Nat. Cell Biol.* **2**, E153 (2000).
19. O. Kerscher, R. Felberbaum, M. Hochstrasser, *Annu. Rev. Cell Dev. Biol.* **22**, 159 (2006).
20. D. S. Kirkpatrick, C. Denison, S. P. Gygi, *Nat. Cell Biol.* **7**, 750 (2005).
21. R. Geiss-Friedlander, F. Melchior, *Nat. Rev. Mol. Cell Biol.* **8**, 947 (2007).
22. R. A. Festa, M. J. Pearce, K. H. Darwin, *J. Bacteriol.* **189**, 3044 (2007).
23. R. Chenna *et al.*, *Nucleic Acids Res.* **31**, 3497 (2003).

24. We thank S. Ehrt, D. Ladant, V. Miller, and A. Steyn for plasmids used in this study. We are grateful to C. Arias and C. Perez for advice on pulse-labeling experiments and to T. Huang, I. Mohr, and M. Pagano for helpful discussions. We thank A. Darwin and M. Pagano for critical review of this manuscript. This work was supported by NIH grants AI065437 and HL092774 (to K.H.D.) and GM67945, HG3456, and HG3616 (to S.P.G.). M.J.P. was supported by grant 5T32AI07189-25.

Supporting Online Material

www.sciencemag.org/cgi/content/full/1163885/DC1
Materials and Methods
Figs. S1 to S8
Table S1

28 July 2008; accepted 16 September 2008
Published online 2 October 2008;
10.1126/science.1163885
Include this information when citing this paper.

Genome of an Endosymbiont Coupling N_2 Fixation to Cellulolysis Within Protist Cells in Termite Gut

Yuichi Hongoh,[1*†] Vineet K. Sharma,[2,3*] Tulika Prakash,[2,3] Satoko Noda,[1] Hidehiro Toh,[2,3] Todd D. Taylor,[2,3] Toshiaki Kudo,[1‡] Yoshiyuki Sakaki,[2§] Atsushi Toyoda,[2,4†] Masahira Hattori,[2,5] Moriya Ohkuma[1]

Termites harbor diverse symbiotic gut microorganisms, the majority of which are as yet uncultivable and their interrelationships unclear. Here, we present the complete genome sequence of the uncultured Bacteroidales endosymbiont of the cellulolytic protist *Pseudotrichonympha grassii*, which accounts for 70% of the bacterial cells in the gut of the termite *Coptotermes formosanus*. Functional annotation of the chromosome (1,114,206 base pairs) unveiled its ability to fix dinitrogen and recycle putative host nitrogen wastes for biosynthesis of diverse amino acids and cofactors, and import glucose and xylose as energy and carbon sources. Thus, nitrogen fixation and cellulolysis are coupled within the protist's cells. This highly evolved symbiotic system probably underlies the ability of the worldwide pest termites *Coptotermes* to use wood as their sole food.

The Formosan subterranean termite *Coptotermes formosanus* is one of the most destructive species, causing severe economic damage in temperate and subtropical regions worldwide (*1*). *C. formosanus* annually costs residents about 1 billion dollars in the United States (*2*) and several hundred million dollars in Japan (*3*). Termites are keystone animals in the global carbon cycle (*4*), and their ability to digest lignocellulose is being explored to promote the development of novel biofuels from woody biomass (*5*). The mechanism underlying the ability of the termites to thrive solely on such a recalcitrant and nitrogen-poor food source as wood remains unclear. Although this capacity has long been attributed to the termite's symbionts, the interrelationships are complex and the organisms resistant to available culture techniques (*6*, *7*).

Hence, we attempted to acquire the complete genome sequence of a prokaryote belonging to the order Bacteroidales, and called phylotype CfPt1-2, which lives specifically within the cells of the uncultivable, cellulolytic protist *Pseudotrichonympha grassii* found in the gut of *C. formosanus* (*8*) (fig. S1). About 1×10^5 CfPt1-2 cells are housed within a single *P. grassii* cell, contributing, in total, 70% of the bacterial cells in the gut of *C. formosanus* (*8*). The parabasalid host *P. grassii* is the most important and indispensable protist species and is essential for the degradation of wood particles in the gut of *C. formosanus* (*9*). *Pseudotrichonympha* species harboring the Bacteroidales endosymbionts are widely distributed among diverse subterranean termites (family Rhinotermitidae) (*10*) (fig. S2). Thus, elucidation of the metabolic functions of CfPt1-2 is crucial for understanding the symbiotic mechanism in *C. formosanus* and other subterranean termites.

A single cell of *P. grassii* was physically isolated from the gut microbiota, and 10^3 to 10^4 cells of its endosymbionts were collected by rupturing the host membrane in buffer (*11*). The collected cells were subjected to isothermal whole-genome amplification for sequence analysis. From the amplified sample, a single circular 1,114,206–base pair (bp) chromosome was unambiguously reconstructed (fig. S3). The chromosome contains 758 putative protein-coding sequences (CDSs), 38 transfer RNA genes, and 4 ribosomal RNA genes (table S1 and S2). The rRNA genes do not constitute an operon, and a region containing the 16*S* rRNA gene and tRNA-Ile gene has been duplicated (*12*). Phylogenetic analysis based on concatenated sequences of ribosomal proteins confirmed that this bacterium belongs to the order Bacteroidales (fig. S4).

Additionally, four circular plasmids were reconstructed (table S1 and fig. S5). Three of the four showed synteny with each other (fig. S6), as well as with the chromosome region 974,000 to 1,042,400 (fig. S7) (*12*). This 68.4-kb–long chromosome region contains three to four duplications of the plasmid-derived sequences. These insertions and duplications imply active rearrangements in this genome. Genes involved in DNA repair and recombination are relatively abundant compared with other known intracellular symbionts (table S3).

The predicted metabolic pathways of CfPt1-2 are shown in Fig. 1. The most striking feature of this bacterium that we uncovered in this study was its ability to fix dinitrogen. The genes encoding nitrogenase (NifHDK), Mo-Fe cofactor biosynthesis proteins, *nif*-operon regulator NifA, and Mo^{2+}-transporter, all of which are essential for N_2 fixation, were identified on the chromosome (table S4 and fig. S8). Although N_2-fixing activity has been demonstrated in diverse termites, including *C. formosanus* (*13*, *14*), the discovery of the requisite genes in a member of the Bacteroidetes was unexpected, because there have been no previous reports of nitrogenase genes in this phylum.

The *nifH* gene of CfPt1-2 was phylogenetically affiliated with a cluster of clones previously obtained from termite guts (*14*, *15*) (fig. S9). It showed only low sequence similarity to the *nifH* genes of any known bacterial species, including the N_2-fixing spirochetes isolated from termite guts (*16*). The expression of the *nifH* gene of CfPt1-2 in the gut was confirmed by reverse-transcription polymerase chain reaction using universal primers for *nifH*. Ninety of 91 sequenced clones were identical or nearly identical to CfPt1-2 *nifH*, which suggests that this bacterium is the principal N_2-fixer in *C. formosanus* gut (*12*). A genus and species, "*Candidatus* Azobacteroides pseudotrichonymphae," is proposed here for the CfPt1-2 bacterium (*12*).

In CfPt1-2, the predicted pathways suggest that the fixed nitrogen, in the form of NH_3, is assimilated initially by the activity of glutamine synthetase and then used for biosynthesis of diverse amino acids and cofactors (Fig. 1). This bacterium also possesses a gene encoding an ammonium transporter and a gene cluster encoding urease and a urea transporter. The orthologs of the latter genes have never previously been found in the Bacteroidales order. The ability to import and assimilate ammonium and urea implies that CfPt1-2 not only fixes atmospheric nitrogen but also recycles the putative nitrogen waste products of parabasalid protists (*17*). The amount of nitrogen in the diet alters the N_2-fixation activity of *C. formosanus* (*13*), possibly because CfPt1-2 can repress N_2 fixation and recycle urea and ammonia when these are abundant in the host cytoplasm. N_2 fixation requires a large amount of energy and thus its regulation is important.

CfPt1-2 possesses genes for using monosaccharides derived from lignocellulose, that is, glucose, xylose, and hexuronates, which are likely to be abundant in the cytoplasm of the cellulolytic host protist. In addition, the genome encodes enzymes involved in a glycogen cycle for storing carbohydrates. Thus, CfPt1-2 is unlikely to experience energy and carbon starvation unless the termite host itself is starved. CfPt1-2 retains a glycolytic pathway, and energy production is achieved through fermentation of sugars to acetate and by fumarate respiration (Fig. 1). Because the genome lacks genes for

[1]Ecomolecular Biorecycling Science Research Team, RIKEN Advanced Science Institute, Saitama 351-0198, Japan. [2]RIKEN Genomic Sciences Center, Kanagawa 230-0045, Japan. [3]MetaSystems Research Team, RIKEN Advanced Science Institute, Kanagawa 230-0045, Japan. [4]Comparative Genomics Laboratory, National Institute of Genetics, Shizuoka 411-8540, Japan. [5]Department of Computational Biology, Graduate School of Frontier Sciences, University of Tokyo, Chiba 277-8561, Japan.

*These authors contributed equally to this work.
†To whom correspondence should be addressed. E-mail: yhongo@riken.jp; atoyoda@lab.nig.ac.jp
‡Present address: Faculty of Fisheries, Nagasaki University, Nagasaki 852-8521, Japan.
§Present address: Toyohashi University of Technology, Aichi 441-8580, Japan.

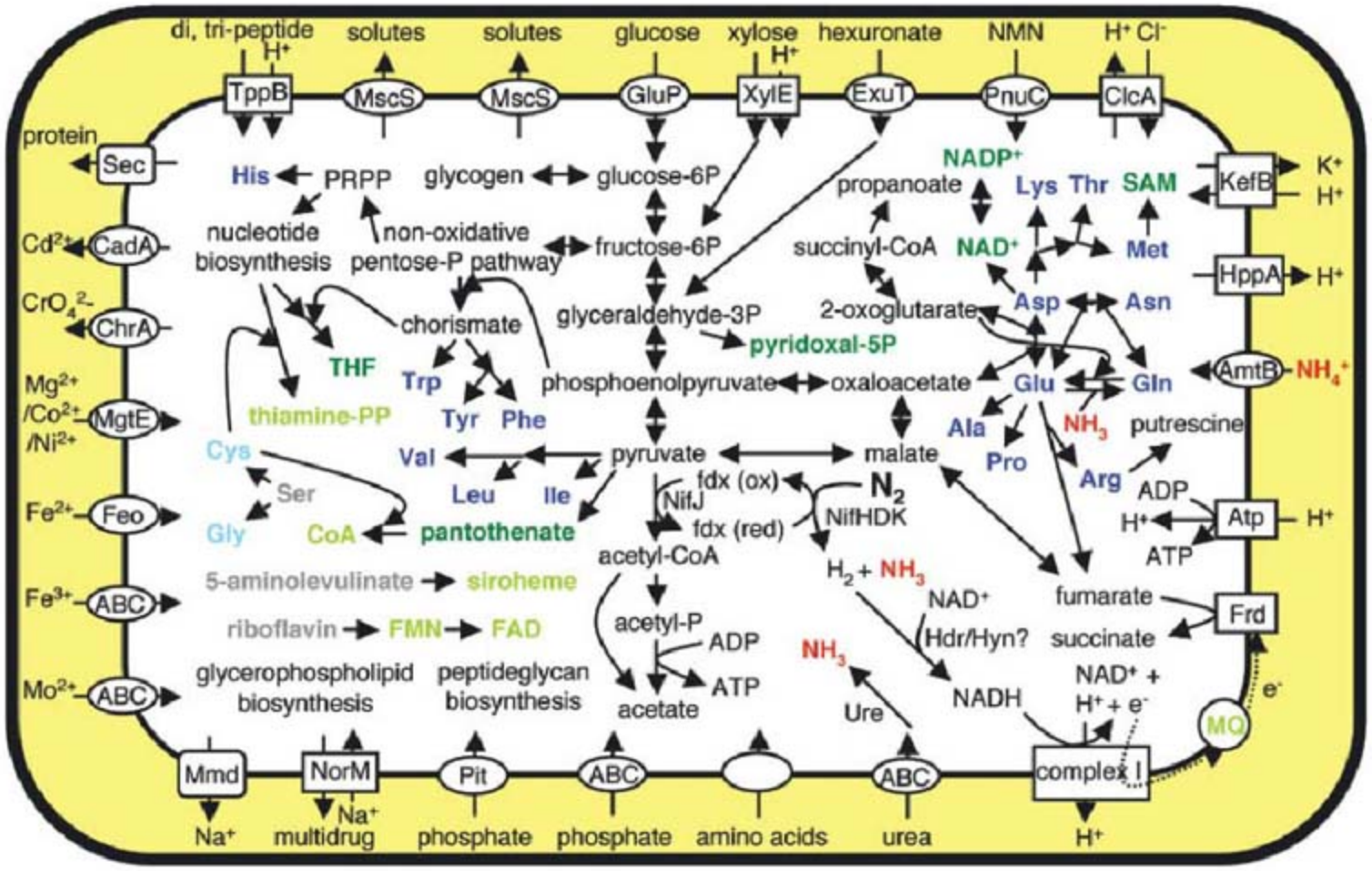

Fig. 1. Predicted metabolic pathways of phylotype CfPt1-2. Blue, synthesized amino acids; green, cofactors. Amino acids and cofactors that can be synthesized from imported precursors are shown in pale colors. The genome encodes pathways for biosynthesis of 19 amino acids. Compounds that should be imported are shown in gray. Provision of menaquinone (MQ) or its precursor 1,4-dihydroxy-2-naphthoate is probably required for fumarate respiration.

catalase, superoxide dismutase, and cytochrome oxidase, CfPt1-2 is strictly anaerobic and cannot use O_2 as an electron acceptor.

Interestingly, this bacterium is known to take up hydrogen (*18*), although no typical hydrogenase gene exists in its genome. The candidates for this function form a cluster of seven genes, including homologs of heterodisulfide reductase and hydrogenase-like components (fig. S10). Molecular H_2 is abundantly produced during both lignocellulose fermentation and N_2 fixation, and is an ideal alternative energy source. Moreover, the removal of excess H_2 theoretically promotes both lignocellulose fermentation and N_2 fixation (fig. S11).

Comparison of the CfPt1-2 genome with those of other known Bacteroidales show that its guanine/cytosine content and CDS density are lower, the number of pseudogenes is larger, and its genome size is smaller (table S5). Although genes involved in nitrogen metabolism have been abundantly retained, CfPt1-2 has no genes encoding extracellular glycosylhydrolases, has few genes for biosynthesis of lipopolysaccharide for a cell wall, and possesses only a few regulatory genes. All of these genes are numerous in Bacteroidales human gut symbionts such as *Bacteroides thetaiotaomicron* (*19*). Although the profile of orthologous groups of CfPt1-2 proteins greatly differs from those of other Bacteroidales, it is strikingly similar to that of phylotype Rs-D17 in the candidate phylum Termite Group 1 (TG1), a bacterial endosymbiont of the cellulolytic protist *Trichonympha agilis* found in the gut of the termite *Reticulitermes speratus* (*20*) (fig. S12). The TG1 endosymbiont also has a reduced and streamlined genome specialized for biosynthesis of amino acids and cofactors (*20*), but unlike CfPt1-2, TG1 cannot fix N_2.

Endosymbionts of cellulolytic protists are probably required by their protist hosts for the biosynthesis of nitrogen compounds that are deficient in woody materials. The cellulolytic protist with its N_2-fixing endosymbionts, in turn, enables highly efficient growth of the host termite and its colony without being limited by nitrogen deficiency. The combined metabolic capacity of these organisms has allowed termites to take advantage of a nutrient-limited resource to humankind's detriment.

References and Notes

1. N. Y. Su, *Sociobiology* **41**, 7 (2003).
2. A. R. Lax, W. L. A. Osbrink, *Pest Manag. Sci.* **59**, 788 (2003).
3. K. Tsunoda, *Sociobiology* **41**, 27 (2003).
4. A. Sugimoto, D. E. Bignell, J. Macdonald, in *Termites: Evolution, Sociality, Symbioses, Ecology*, T. Abe, D. E. Bignell, M. Higashi, Eds. (Kluwer Academic Publishers, Netherlands, 2000), pp. 409–436.
5. F. Warnecke *et al.*, *Nature* **450**, 560 (2007).
6. M. Ohkuma, *Trends Microbiol.* **16**, 345 (2008).
7. N. Shinzato, M. Muramatsu, T. Matsui, Y. Watanabe, *Biosci. Biotechnol. Biochem.* **69**, 1145 (2005).
8. S. Noda *et al.*, *Appl. Environ. Microbiol.* **71**, 8811 (2005).
9. T. Yoshimura, *Wood Res.* **82**, 68 (1995).
10. S. Noda *et al.*, *Mol. Ecol.* **16**, 1257 (2007).
11. Materials and methods are available as supporting material on *Science* Online.
12. See SOM Text.
13. J. A. Breznak, W. J. Brill, J. W. Mertins, H. C. Coppel, *Nature* **244**, 577 (1973).
14. M. Ohkuma, S. Noda, T. Kudo, *Appl. Environ. Microbiol.* **65**, 4926 (1999).
15. S. Noda, M. Ohkuma, T. Kudo, *Microbes Environ.* **17**, 139 (2002).
16. T. G. Lilburn *et al.*, *Science* **292**, 2495 (2001).
17. J. M. Carlton *et al.*, *Science* **315**, 207 (2007).
18. J. Inoue, K. Saita, T. Kudo, S. Ui, M. Ohkuma, *Eukaryot. Cell* **6**, 1925 (2007).
19. J. Xu *et al.*, *PLoS Biol.* **5**, e156 (2007).
20. Y. Hongoh *et al.*, *Proc. Natl. Acad. Sci. U.S.A.* **105**, 5555 (2008).

21. We are grateful to all the technical staff of the Sequence Technology Team at RIKEN Genomic Sciences Center (GSC) and the Ecomolecular Biorecycling Science Research Team for their assistance. This work was supported in part by a grant for the President's Discretionary Fund of RIKEN; a Special Fund for RIKEN GSC; grants for the Bioarchitect Research Program and the Eco Molecular Science Research Program from RIKEN; a Discovery Research Institute Research Grant to Y.H. from RIKEN; a Grant-in-Aid for Scientific Research on Priority Areas "Comprehensive Genomics" from the Ministry of Education, Culture, Sports, Science, and Technology of Japan to M.H.; and a Grant-in-Aid for Scientific Research from Japan Society for the Promotion of Science to Y.H. and M.O. The authors declare no competing financial interests. The sequence data have been deposited in GenBank/DDBJ/EMBL under accession numbers AP010656-60.

Supporting Online Material

www.sciencemag.org/cgi/content/full/322/5904/1108/DC1
Materials and Methods
SOM Text
Figs. S1 to S12
Tables S1 to S7
References

5 September 2008; accepted 8 October 2008
10.1126/science.1165578

Globally Distributed Uncultivated Oceanic N_2-Fixing Cyanobacteria Lack Oxygenic Photosystem II

Jonathan P. Zehr,[1]* Shellie R. Bench,[1] Brandon J. Carter,[1] Ian Hewson,[1] Faheem Niazi,[2] Tuo Shi,[1] H. James Tripp,[1] Jason P. Affourtit[2]

Biological nitrogen (N_2) fixation is important in controlling biological productivity and carbon flux in the oceans. Unicellular N_2-fixing cyanobacteria have only recently been discovered and are widely distributed in tropical and subtropical seas. Metagenomic analysis of flow cytometry–sorted cells shows that unicellular N_2-fixing cyanobacteria in "group A" (UCYN-A) lack genes for the oxygen-evolving photosystem II and for carbon fixation, which has implications for oceanic carbon and nitrogen cycling and raises questions regarding the evolution of photosynthesis and N_2 fixation on Earth.

Biological N_2 fixation (BNF) is catalyzed by the enzyme nitrogenase, which is present in diverse Bacteria and Archaea (*1*). Marine BNF is particularly important in the oligotrophic open-ocean gyres, where nitrogen (N) inputs to stratified surface waters are stoichiometrically related to photosynthetic carbon (C) fixation and the vertical export of C to the deep ocean (*2*). Biogeochemically based estimates of oceanic N_2 fixation rates are much higher than previously believed (*2*–*5*). Oceanic BNF was assumed to be primarily due to the filamentous cyanobacteria *Trichodesmium* (*6*, *7*) and the symbiotic filamentous cyanobacteria *Richelia* (*8*, *9*), until the recent discovery that oceanic unicellular cyanobacteria are important in oceanic N_2 fixation (*10*, *11*). The unicellular N_2-fixing cyanobacteria were initially discovered only by amplification of nitrogenase genes and gene transcripts (mRNA) from oceanic water samples (*12*, *13*), because they cannot be detected with traditional net collection methods and microscopy as can *Trichodesmium* and *Richelia*.

One phylogenetic group of unicellular N_2-fixing cyanobacterial nitrogenase gene sequences ("group A" or UCYN-A *nifH*) (*13*) is most closely related to sequences from the marine unicellular cyanobacterium *Cyanothece* sp. strain ATCC 51142, a marine strain isolated from an intertidal habitat, and to those of the unicellular cyanobacterial symbiont of the diatom *Rhopalodia gibba* (*14*). UCYN-A *nifH* gene sequences have been reported from the Atlantic and Pacific Oceans (*15*), but UCYN-A cyanobacteria have not been successfully cultivated despite repeated attempts. These microorganisms express nitrogenase genes with maximum transcript abundances during the light period (*11*, *16*). The daytime expression of nitrogenase presents an enigma, because the enzyme is inactivated by oxygen evolved during photosynthesis. Most cyanobacteria use temporal or spatial separation of photosynthesis and N_2 fixation to prevent nitrogenase inactivation (*17*). However, we found that UCYN-A cyanobacteria have a genotype not previously known in free-living cyanobacteria and are genetically incapable of oxygenic photosynthesis, which also explains why they can fix N_2 during daylight.

We initially assumed that the UCYN-A cyanobacteria would have cell diameters of 2 to 8 μm, similar to those of typical coastal (*Cyanothece*) and oceanic (*Crocosphaera watsonii*, UCYN-B) cyanobacteria (*18*), but discovered that the UCYN-A cells were less than 1 μm in diameter (*19*). Natural populations of UCYN-A cells could not be completely separated from other small phototrophic and heterotrophic populations by flow cytometry (FCM), but highly enriched cell sorts were obtained by screening cells sorted by fluorescence-activated cell sorting (FACS) for UCYN-A *nifH* genes with a quantitative real-time fluorescence polymerase chain reaction (QPCR) assay, Real-Time TaqMan (*16*, *20*). We refined sort parameters (fig. S1) from those we previously used (*19*) to sort natural populations of UCYN-A cells from numerous North and South Pacific Ocean water samples (Fig. 1). We found that the populations are widely distributed, which indicated that our sorting strategy for UCYN-A cells was robust (table S2).

Amplification of 16*S* ribosomal RNA (rRNA) genes from the sorted cells, using PCR with universal 16*S* rRNA primers, showed that the sorted population contained some noncyanobacterial Bacteria (such as *Pelagibacter ubique*) and non–N_2-fixing cyanobacteria (*Prochlorococcus* and *Synechococcus*) in addition to the UCYN-A cyanobacteria (table S1). The per-

[1]Ocean Sciences Department, University of California, Santa Cruz, 1156 High Street, Santa Cruz, CA 95064, USA. [2]454 Life Sciences, 20 Commercial Street, Branford, CT 06405, USA.

*To whom correspondence should be addressed. E-mail: zehrj@ucsc.edu

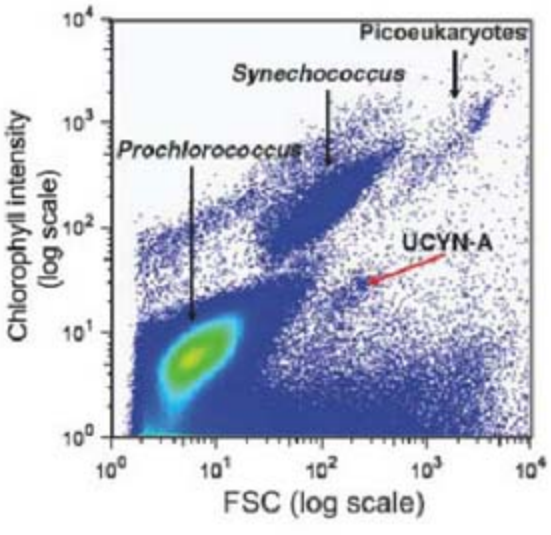

Fig. 1. Cytogram of the forward scatter (*x* axis) and chlorophyll fluorescence (*y* axis) profile from concentrated water samples collected from a depth of 15 m at Station ALOHA (North Pacific) in late January 2008. The UCYN-A population sorted for MDA genome amplification and subsequent sequencing indicated by the red arrow.

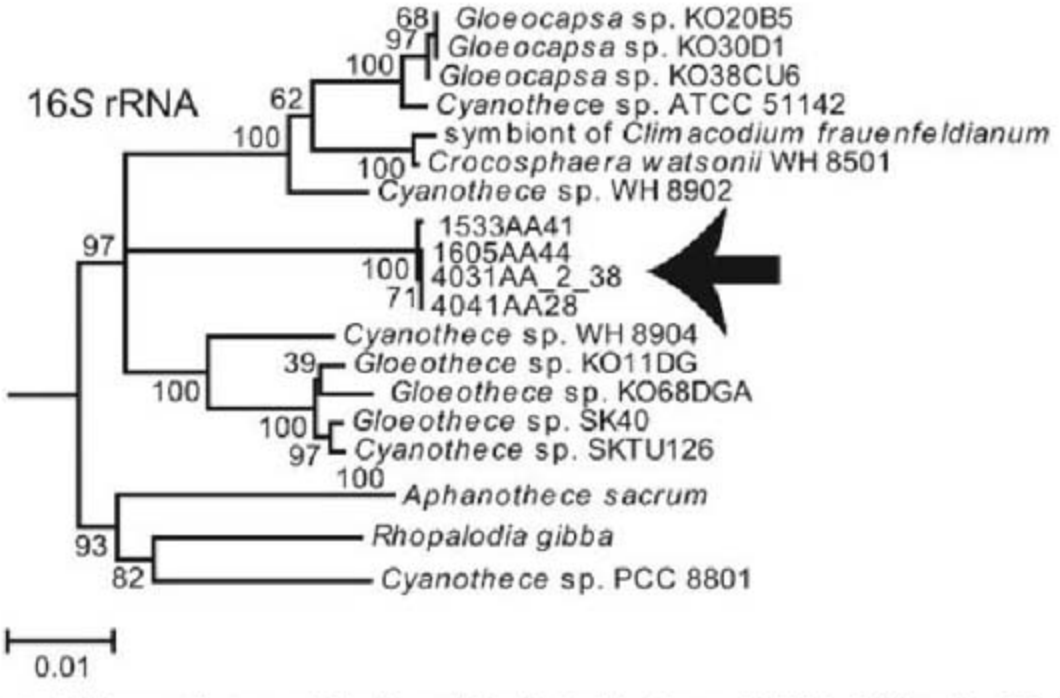

Fig. 2. Phylogenetic tree of North and South Pacific Ocean UCYN-A full-length 16*S* rRNA nucleotide gene sequences showing the relationship of UCYN-A to *Cyanothece* sp. ATCC 51142 and other unicellular cyanobacteria. The arrow indicates the UCYN-A group.

centage of UCYN-A cells in the defined sort region varied depending on the source of the (tables S1 and S2).

All 16*S* rRNA, *nifH*, and *nifD* sequences amplified from sorted cells were consistent with the UCYN-A cells being *Cyanothece*-like unicellular N_2-fixing cyanobacteria (*13*) (Fig. 2 and figs. S2 and S3) even though they were much smaller. The 16*S* rRNA *Cyanothece*-like sequence was linked to the UCYN-A *nifH* gene by FACS-sorting single cells and multiplex gene amplification (fig. S2) of *nifH* and 16*S* rRNA genes from individual cells in which the positive single-cell QPCR reaction mixtures for *nifH* were used as a template for the second 16*S* rRNA amplification (*21*). Reactions that were negative for UCYN-A *nifH* were also negative for unicellular N_2-fixing cyanobacterial 16*S* rRNA (fig. S2).

A water sample collected from a depth of 15 m at the North Pacific Ocean long-term monitoring site Station ALOHA in late January 2008 (during Hawaii Ocean Time-series cruise HOT 199) indicated the presence of a high proportion (51%) of UCYN-A cells (Fig. 1). We used this population for metagenomic analysis, using Titanium sequencing technology from 454 Life Sciences (*21*). Multiple displacement amplification (MDA) (*21*) of DNA from approximately 5000 sorted cells was used to generate a genomic shotgun library that we estimate gave at least 10-fold genomic coverage of the 2- to 3-Mb UCYN-A genome in approximately 400,000 sequence reads (assuming that roughly one-third of the reads in the run were not UCYN-A). 177,834 sequence reads were most similar to the N_2-fixing unicellular cyanobacteria *Cyanothece* sp. ATCC 51142, *Cyanothece* sp. CCY 0110, or *C. watsonii* WH 8501, on the basis of a BLAST analysis (*21*), whereas only 40,593 sequences had best BLAST hits to *Prochlorococcus* proteins, and 96,341 sequences were most similar to proteins from other microorganisms, including noncyanobacterial Bacteria. The 16*S* rRNA sequences also showed that the library was dominated by UCYN-A DNA sequences (Fig. 3), and they agreed with the QPCR data for UCYN-A cyanobacteria. The sequence read library represented good coverage of the UCYN-A genome because it contained the entire nitrogenase gene cluster on one assembled contig (Fig. 4) (*21*). The nitrogenase gene arrangement and composition were very similar to those of *Cyanothece* sp. ATCC 51142 and of the *R. gibba* symbiont (Fig. 4). Most of the proteins in the common cyanobacterial genome core (*22*) were identified by BLAST. Comparison of sequences to the cyanobacterial genome core (*21*) indicated that at least 79% of the core cyanobacterial genome had been sampled (fig. S4).

Although the core genes and all the *nif* genes were present, no candidate UCYN-A sequences were found that corresponded to C fixation, C concentration, or photosystem II (PSII) and associated pigments (such as phycoerythrin or phycobiliprotein linker). However, good coverage of candidate UCYN-A PSI genes was obtained (Fig. 5). In comparison, we had equal coverage of *Prochlorococcus* PSI and PSII genes, although they were a much smaller component of the sequence library (Fig. 5). However, we did detect a complete PSI *psaA* gene, found on one single assembled contig [5788 base pairs (bp) assembled from 948 sequence reads], followed immediately by 1857 bp of the *psaB* gene, which clustered with sequences from other unicellular N_2-fixing cyanobacteria (fig. S3). No unicellular N_2-fixing cyanobacteria phycoerythrin or phycocyanin genes (or associated linkers) were found in the metagenome, which is consistent with the observation that UCYN-A cyanobacteria were not detected by phycoerythrin fluorescence in FCM (*19*). Additional PCR experiments readily amplified the UCYN-A PSI genes found on the genomic contig, but no C fixation or PSII genes were obtained. We obtained further evidence that UCYN-A lack PSII genes by amplifying photosynthetically critical genes using degenerate PCR primers (*21*). From

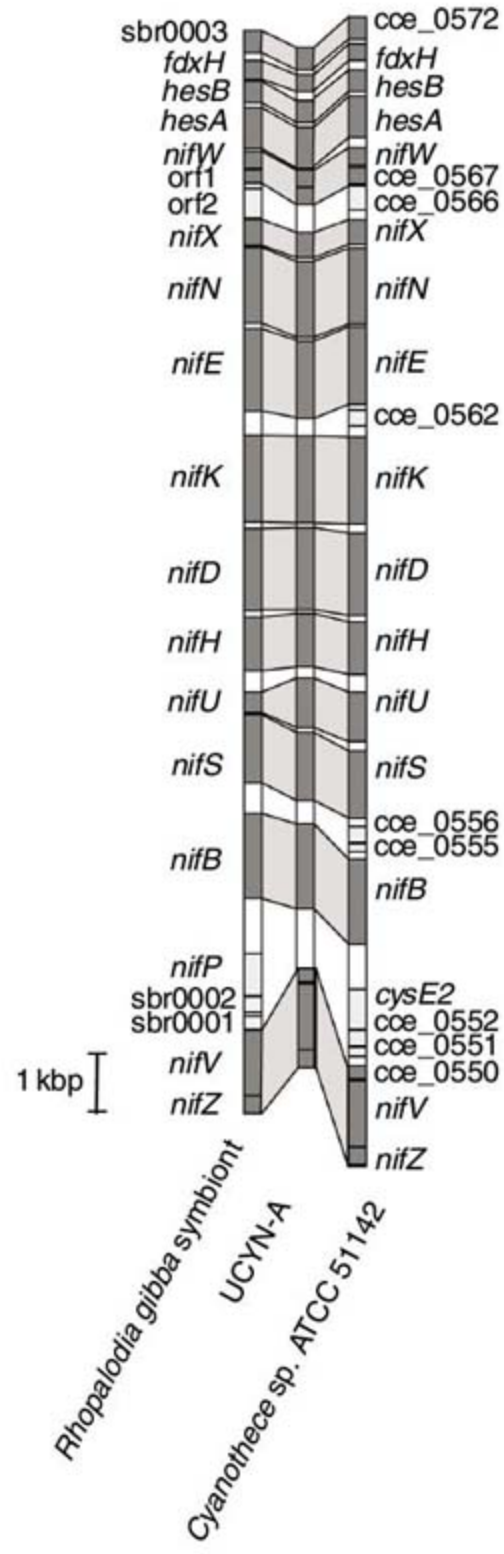

Fig. 4. Comparison of the UCYN-A *nif* gene cluster to those of *Cyanothece* sp. ATCC 51142 and the *R. gibba* symbiont. The *nif* cluster was located on a large (135,849 bp) contig assembled from 5161 sequence reads. The figure shows the synteny of approximately 23 kbp of coding sequences for the *nif* gene clusters of UCYN-A (contig 02671, NCBI accession no. FJ170277), a N_2-fixing endosymbiont of *R. gibba* (NCBI accession no. AY728387), and the circular chromosome of *Cyanothece* sp. ATCC 51142 (EMBL accession no. CP000806). Genes with full-length matches of amino acid sequence are shown in dark gray, genes with no matches are shown in light gray, and noncoding DNA is shown in white.

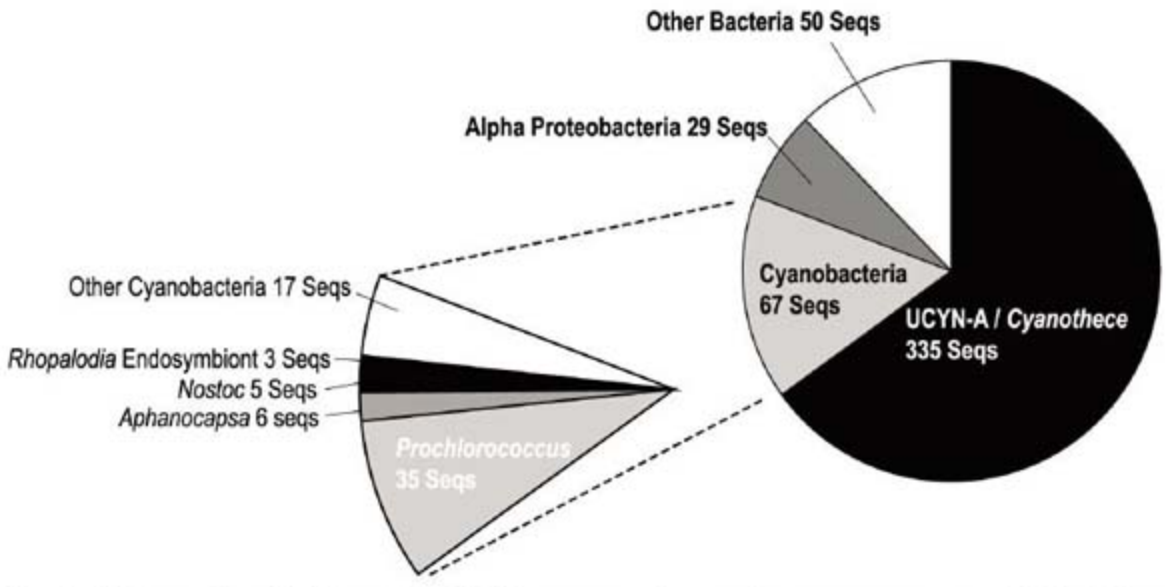

Fig. 3. Phylogenetic affiliation of 16*S* rRNA sequences from metagenome sequences obtained from the station ALOHA 15-m sample. Sequences matching 16*S* rRNA were first retrieved by comparing the metagenome reads against those of the Ribosomal Database Project. Matching sequences were then assigned phylogenetically by BLASTn comparison to the nonredundant database at the National Center for Biotechnology Information (NCBI).

multiple samples of sorted cells, we successfully amplified UCYN-A *psaA* fragments with DNA sequences >98% identical to those genes found on the genomic contigs. However, attempts to amplify genes for the PSII D1 protein (*psbA*) as well as the RuBisCO large subunit yielded only sequences that were >98% identical to those of *Prochlorococcus* or >94% identical to those of *Synechococcus* species, and none that were similar to those of unicellular diazotrophs, as expected for UCYN-A sequences. The absence of any candidate UCYN-A PSII genes is clear, given the random and complete coverage of the sequencing effort, the high percentage of genome core coverage, the lack of amplification when degenerate primers were used, and the random location of photosynthesis genes in cyanobacterial genomes (*23*). Although it has been shown that some cyanobacteria can uncouple PSI from PSII using either organic (*24*) or inorganic (*25*) substrates as electron donors, this is the first observation of a cyanobacterium that completely lacks the PSII apparatus. This conclusion is striking because there are no reports to our knowledge of free-living cyanobacteria that are not oxygenic phototrophs.

The UCYN-A phylogeny and poor pigmentation (dim chlorophyll fluorescence) resemble those seen in observations of the *R. gibba* symbiont (*14*). Although the *R. gibba* symbiont sequences are no closer to UCYN-A sequences phylogenetically than to those of other cyanobacteria in the unicellular N_2-fixing cyanobacterial lineage (Fig. 2 and fig. S3), the symbiont of *R. gibba* also appears to have lost photosynthetic capabilities and pigmentation (*14*, *26*). In the *R. gibba* symbiont, some of the PSII proteins (*psbC* and *psbD*) have become pseudogenes (*14*, *26*). We did not detect UCYN-A cells in association with large cells, neither in size-fractionation filtration nor by FCM, and it appears to be a free-living organism.

Our work shows that oceanic UCYN-A cyanobacteria are missing the entire PSII apparatus, although the PSI apparatus appears to be intact (Fig. 5). It is possible that UCYN-A cyanobacteria are photoheterotrophic cells that generate adenosine triphosphate with PSI and are not able to fix C by the Calvin-Benson-Basham cycle as oxygenic photoautotrophs do. It is unclear how PSI functions in the absence of PSII. The UCYN-A strain, like the *R. gibba* symbiont, fixes N_2 during the daytime, judging by its nitrogenase gene expression pattern (*11*). The lack of a functional PSII in the UCYN-A cells means that nitrogenase will not be poisoned by oxygen evolved from photosynthesis. The lack of oxygenic photosynthesis in UCYN-A cells has implications for C and N cycling in the oceans, as well as for the evolution of photosynthesis and N_2 fixation. UCYN-A cyanobacteria overlap in size and fluorescence characteristics with non–N_2-fixing microbial populations in the open ocean, including *Prochlorococcus*, *Synechococcus*, and other Bacteria, making them difficult to detect and quantify in the oceanic picoplankton. However, unicellular cyanobacteria may have a substantial impact on the N budget (*10*, *11*), particularly in this case, because N_2 fixation is not linked to C fixation. It is critical to determine the global importance of N_2 fixation by this unusual photoheterotrophic cyanobacterial group in order to better constrain the global ocean N budget.

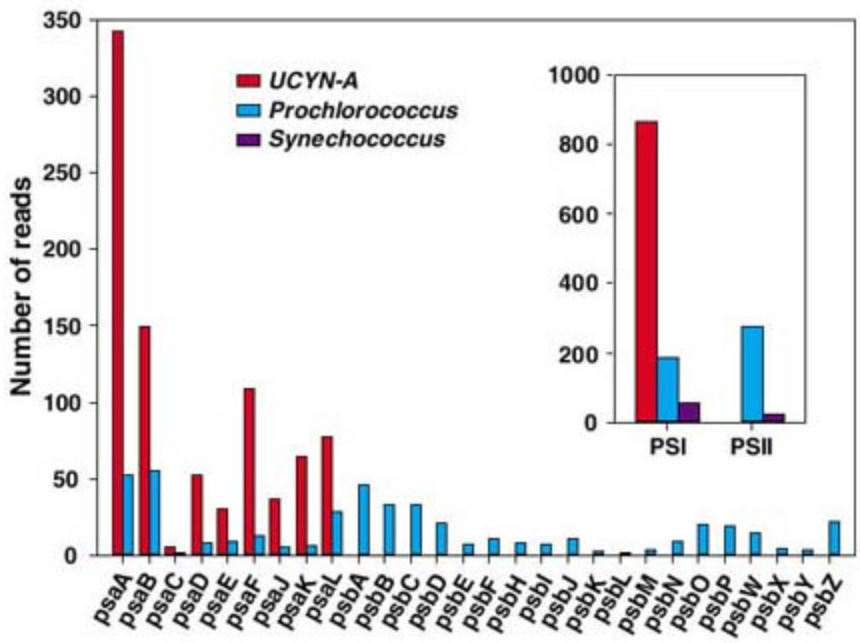

Fig. 5. Photosystem genes identified from sequencing of FACS-sorted environmental samples. The distribution of the number of sequence reads having top BLAST matches to individual photosystem genes in metagenomes of UCYN-A and *Prochlorococcus* is shown. Candidate UCYN-A photosystem sequences were identified by screening for reads having top BLAST matches to photosystem genes in *Cyanothece*, *Crocosphaera watsonii* WH8501, and *Synechocystis*, which are phylogenetically related to UCYN-A and hence collectively represent a proxy of the UCYN-A metagenome. The inset shows the distribution of the total number of PSI and PSII genes identified in metagenomes of UCYN-A, *Prochlorococcus*, and marine *Synechococcus*.

References and Notes

1. J. P. W. Young, in *Genomes and Genomics of Nitrogen-Fixing Organisms*, R. Palacios, W. E. Newton, Eds. (Springer Netherlands, Dordrecht, Netherlands, 2005), vol. 3, pp. 221–241.
2. C. Mahaffey, A. F. Michaels, D. G. Capone, *Am. J. Sci.* **305**, 546 (2005).
3. D. A. Hansell, N. R. Bates, D. B. Olson, *Mar. Chem.* **84**, 243 (2004).
4. A. F. Michaels *et al.*, *Biogeochemistry* **35**, 181 (1996).
5. N. Gruber, J. L. Sarmiento, *Global Biogeochem. Cycles* **11**, 235 (1997).
6. D. G. Capone *et al.*, *Global Biogeochem. Cycles* **19**, GB2024 (2005).
7. J. LaRoche, E. Breitbarth, *J. Sea Res.* **53**, 67 (2005).
8. E. J. Carpenter *et al.*, *Mar. Ecol. Prog. Ser.* **185**, 273 (1999).
9. E. L. Venrick, *Limnol. Oceanogr.* **19**, 437 (1974).
10. J. P. Montoya *et al.*, *Nature* **430**, 1027 (2004).
11. J. P. Zehr *et al.*, *Limnol. Oceanogr.* **52**, 169 (2007).
12. J. P. Zehr *et al.*, *Nature* **412**, 635 (2001).
13. J. P. Zehr, M. T. Mellon, S. Zani, *Appl. Environ. Microbiol.* **64**, 3444 (1998).
14. J. Prechtl, C. Kneip, P. Lockhart, K. Wenderoth, U. G. Maier, *Mol. Biol. Evol.* **21**, 1477 (2004).
15. L. I. Falcón, F. Cipriano, A. Y. Chistoserdov, E. J. Carpenter, *Appl. Environ. Microbiol.* **68**, 5760 (2002).
16. M. J. Church, C. M. Short, B. D. Jenkins, D. M. Karl, J. P. Zehr, *Appl. Environ. Microbiol.* **71**, 5362 (2005).
17. P. Fay, *Microbiol. Rev.* **56**, 340 (1992).
18. J. B. Waterbury, R. Rippka, in *Bergey's Manual of Systematic Bacteriology*, J. T. Staley, M. P. Bryant, N. Pfenning, J. G. Holt, Eds. (Williams & Wilkins, Baltimore, MD, 1989), vol. 3, pp. 1728–1729.
19. N. L. Goebel *et al.*, *J. Phycol.* **44**, 1212 (2008).
20. M. J. Church, B. D. Jenkins, D. M. Karl, J. P. Zehr, *Aquat. Microb. Ecol.* **38**, 3 (2005).
21. Materials and methods are available as supporting material on *Science* Online.
22. T. Shi, P. Falkowski, *Proc. Natl. Acad. Sci. U.S.A.* **105**, 2510 (2008).
23. T. Shi, T. S. Bibby, L. Jiang, A. J. Irwin, P. Falkowski, *Mol. Biol. Evol.* **22**, 2179 (2005).
24. H. S. Misra, N. P. Khairnar, S. K. Mahajan, *J. Plant Physiol.* **160**, 33 (2003).
25. Y. Cohen, B. B. Jorgensen, N. P. Revsbech, R. Poplawski, *Appl. Environ. Microbiol.* **51**, 398 (1986).
26. C. Kneip, C. Vobeta, P. Lockhart, U. Maier, *BMC Evol. Biol.* **8**, 30 (2008).

27. We thank J. Montoya, D. Karl, M. J. Church, J. K. Doggett, the Hawaii Ocean Time-series crew, and the captain and crew of the R/V *Kilo Moana* for facilitating sample collection and analysis. We also thank E. Mondragon, P. Moisander, M. Hogan, K. Pennebaker, R. Beinart, and the Zehr laboratory for technical support. This work was partially supported by the Gordon and Betty Moore Foundation [J.P.Z. and the Microbial Environmental Genomics: Modeling, Experimentation and Remote Sensing (MEGAMER) facility], NSF (OCE0425363) (J.P.Z.), and the NSF Center for Microbial Oceanography Research and Education (CCF424599) (J.P.Z.). Support for sequencing was provided by 454 Life Sciences, a Roche Company. The GenBank accession numbers of the sequences generated from PCR in this study are EU187504 to EU187629 and FJ189800 to FJ190047. For a complete list of GenBank accessions, please see the supporting online material (*21*).

Supporting Online Material

www.sciencemag.org/cgi/content/full/322/5904/1110/DC1

Materials and Methods
References
Figs. S1 to S4
Tables S1 and S2

2 September 2008; accepted 2 October 2008
10.1126/science.1165340

Arabidopsis Stomatal Initiation Is Controlled by MAPK-Mediated Regulation of the bHLH SPEECHLESS

Gregory R. Lampard,* Cora A. MacAlister,* Dominique C. Bergmann†

Stomata, epidermal structures that modulate gas exchange between plants and the atmosphere, play critical roles in primary productivity and the global climate. Positively acting transcription factors and negatively acting mitogen-activated protein kinase (MAPK) signaling control stomatal development in *Arabidopsis*; however, it is not known how the opposing activities of these regulators are integrated. We found that a unique domain in a basic helix-loop-helix (bHLH) stomatal initiating factor, SPEECHLESS, renders it a MAPK phosphorylation target in vitro and modulates its function in vivo. MAPK cascades modulate a diverse set of activities including development, cell proliferation, and response to external stresses. The coupling of MAPK signaling to SPEECHLESS activity provides cell type specificity for MAPK output while allowing the integration of multiple developmental and environmental signals into the production and spacing of stomata.

In *Arabidopsis*, stomatal fate and pattern are regulated by three closely related basic helix-loop-helix (bHLH) transcription factors—SPEECHLESS (SPCH), MUTE, and FAMA—that, in partnership with the more distantly related bHLHs lCE1/SCREAM and SCREAM2, control initiation of asymmetric divisions, proliferation of transient precursor cells, and differentiation of stomatal guard cells, respectively (fig. S1) (*1*–*4*). Acting in opposition to these stomatal promoting factors are signaling systems that limit stomatal density and establish pattern. These negative regulators include the ERECTA (ER) family of leucine-rich repeat (LRR) receptor–like kinases (*5*, *6*) and the LRR receptor–like protein TOO MANY MOUTHS (TMM) (*7*) that both may work in concert with the putative ligand EPF1 (*8*). A subtilisin protease, SDD1, also negatively regulates stomatal production but may act independently of this receptor-ligand module (*8*, *9*).

Genetic evidence places a mitogen-activated protein kinase (MAPK) signaling cascade downstream of the receptors in stomatal development (*10*, *11*). In all eukaryotes, MAPK cascades control a diverse array of activities, including the regulation of cell division and differentiation and the coordination of responses to environmental inputs (*12*, *13*). The MAPK components implicated in stomatal development (YODA, MKK4/5, and MPK3/6) are broadly expressed (*11*, *14*) and are involved in multiple activities. For example, YODA is required for asymmetric cell divisions in the embryo (*15*), and MKK4/5 and MPK3/6 were initially characterized by their roles in stress and pathogen responses (*16*, *17*). Because of these multiple roles, a major challenge in MAPK signaling is to understand how common signaling elements evoke specific responses. Spatially or temporally restricted expression of MAPK substrates could provide this specificity. Developmental MAPK substrates have not been previously described in plants; however, the cell type–specific expression and activities of SPCH, MUTE, and FAMA make these proteins attractive candidates for such specificity factors. Here we show that SPCH is a substrate of MPK3 and MPK6 in vitro, that specific phosphorylation sites on SPCH regulate its activity in vivo, and that known components of the stomatal development signaling network modulate SPCH behavior.

The *SPCH* loss-of-function phenotype is strikingly similar to that caused by constitutive activation of the MAPK pathway components YODA and MKK4/5 (*10*, *11*), and *spch* is epistatic to *yoda* (*2*); these results are consistent with SPCH being a downstream target of MAPKs in the epidermis. To test whether SPCH is regulated by MAPK activity, we examined the expression of transcriptional (*SPCHpro::GFP*) and translational (*SPCHpro::SPCH-GFP*) reporters (GFP, green fluorescent protein) in plants expressing constitutively active (CA) YODA (*YODApro::CA-YODA*) (*11*). At 5 days post-germination (dpg), both wild-type plants (20 of 20) and *YODApro::CA-YODA* plants (19 of 20) expressed *SPCHpro::GFP* (fig. S2, A and B). Wild-type plants also expressed *SPCHpro::SPCH-GFP* (20 of 20), but *YODApro::CA-YODA* plants did not (0 of 20; fig. S2, C and D); this result suggests that YODA does not prevent transcription of *SPCH*, but rather limits the production or abundance of SPCH protein.

Phosphorylation of transcription factors can modulate their levels and activities (*18*, *19*). We tested whether SPCH was an in vitro substrate for phosphorylation by the MAPKs previously implicated in stomatal development (MPK3 and MPK6) (*10*). SPCH, but not its paralogs FAMA and MUTE, could be phosphorylated by both MPK3 and MPK6 (Fig. 1B and fig. S3A). Alignment of SPCH, MUTE, and FAMA proteins reveals high sequence conservation in their bHLH domains and C termini (Fig. 1A) (*2*). However, SPCH also has a unique 93–amino acid domain [herein referred to as the MAPK target domain (MPKTD)] that contains 10 consensus MAPK phosphorylation target sites. Five of these sites

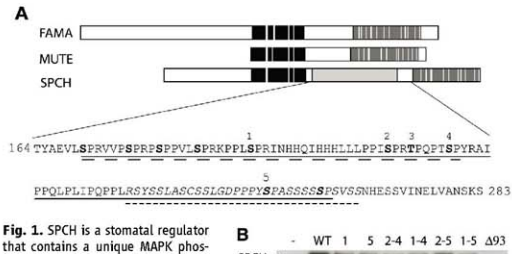

Fig. 1. SPCH is a stomatal regulator that contains a unique MAPK phosphorylation target domain. **(A)** Protein alignment of SPCH, MUTE, and FAMA. Highest conservation is in the bHLH domain (black) and C terminus (dark gray). White lines within these domains indicate nonidentical residues. The sequence of the MPKTD is shown with beginning and ending amino acid residue positions. Deletions are denoted as a solid underline for Δ93, a long-dashed underline for Δ49, and a short-dashed underline for Δ31. Italics denote the predicted PEST sequence. MAPK target sites are in bold. High-stringency sites are denoted 1 (Ser^{193}), 2 (Ser^{211}), 3 (Thr^{214}), 4 (Ser^{219}), and 5 (Ser^{255}). Abbreviations for amino acid residues: A, Ala; C, Cys; D, Asp; E, Glu; G, Gly; H, His; I, Ile; K, Lys; L, Leu; N, Asn; P, Pro; Q, Gln; R, Arg; S, Ser; T, Thr; V, Val; Y, Tyr. **(B)** In vitro activity of recombinant MPK3 (top) and MPK6 (bottom) on bacterially expressed SPCH variants. Lane labels indicate specific SPCH variant tested. Arrows correspond to phosphorylated SPCH and autophosphorylation of MPKs.

Department of Biology, Stanford University, Stanford, CA 94305, USA.

*These authors contributed equally to this work.
†To whom correspondence should be addressed. E-mail: dbergmann@stanford.edu

contain a Pro-X-Ser/Thr-Pro (P-X-S/T-P) motif, marking them as high-stringency sites (*20*) (Fig. 1A). Because SPCH differs from the nonsubstrate MUTE and FAMA proteins primarily in the MPKTD, we performed phosphorylation assays with a version of SPCH lacking the MPKTD and with the MPKTD alone. All MPK3 and MPK6 in vitro phosphorylation target sites appear to be contained within the SPCH MPKTD (Fig. 1B and fig. S3).

We then tested the functional importance of the SPCH MPKTD by using both the strong, broadly expressed 35S promoter and the endogenous SPCH promoter to express full-length SPCH and SPCHΔMPKTD variants in plants. Expression of *35S::SPCH* was previously reported to induce divisions in pavement cells (*2*) and to produce extra stomatal lineage cells (*3*). *35S::SPCH* expression in wild-type plants resulted in additional divisions in pavement cells and a modest increase in total epidermal cell number (Fig. 2B), whereas expression of *SPCHpro::SPCH* in the wild type resulted in no significant phenotypic effects (Fig. 3). In contrast to these results with full-length SPCH, SPCHΔMPKTD variants markedly affected epidermal development. When the entire domain was deleted (*35S::SPCHΔ93* or *SPCHpro::SPCHΔ93*), the epidermis of transformed plants exhibited large clusters of stomata (Fig. 2C and fig. S4), a phenotype similar to that produced by *35S::MUTE* (*2*, *3*). The *SPCHΔ93* results are unsurprising given the strong similarity of SPCH and MUTE—particularly when the MPKTD is removed (Fig. 1A)—and in light of previous reports that overexpression of FAMA deletion variants mimics *35S::MUTE* (*1*).

More informative were the phenotypes induced by expressing a smaller deletion that eliminates eight target sites (four of five high-stringency sites) but leaves the fifth high-stringency site (Ser^{255}) intact (*SPCHΔ49*, Fig. 1A) or the complementary deletion that removes the remaining target sites (*SPCHΔ31*, Fig. 1A). Expression of each deletion variant produced excessive numbers of asymmetric cell divisions in the epidermis, with *SPCHΔ49* producing a stronger but qualitatively similar phenotype to that of *SPCHΔ31* when expressed with the same promoter (Fig. 2D and fig. S4, B to D). The divisions induced by *SPCHΔ49* and *SPCHΔ31* were physically asymmetric and created cells with meristemoid morphology, much like the stomatal lineage–establishing divisions that SPCH promotes during normal development. To better characterize the cells produced by ectopic divisions, we monitored the expression of cell fate markers. Nearly all small, ectopic cells expressed *TMMpro::TMM-GFP*, a general marker of cells in the stomatal lineage (Fig. 2, E and F) (*7*). A smaller fraction expressed *MUTEpro::GFP*, a marker that is normally expressed in meristemoids just before their transition to guard mother cells (GMCs) (*2*). Thus, the population evidently consists of both meristemoids and other stomatal lineage cells (fig. S4H).

The division-promoting behavior of both *SPCHΔ49* and *SPCHΔ31* suggests that multiple residues within the MPKTD are functionally important. To define the specific residues, we repeated the in vitro and in vivo assays with SPCH variants in which the phosphorylatable S/Ts of the five high-stringency phosphorylation sites were substituted with nonphosphorylatable alanines. Each of these S/T → A variants was made as a fusion protein with yellow fluorescent protein (YFP) at the C terminus and was expressed with the SPCH promoter (*21*). Converting all five high-stringency MAPK target residues to alanines (*SPCHpro::SPCH1-5 S/T>A*) resulted in a protein that created ectopic stomata like those created by *SPCHpro::SPCHΔ93* (Fig. 2G). Converting the first four sites to alanines (*SPCHpro::SPCH1-4 S/T>A*) resulted in ectopic division phenotypes similar to those seen with *SPCHpro::SPCHΔ49* (Fig. 2H). The effect of *SPCHpro::SPCH5 S/T>A*, however, was much weaker than that of *SPCHpro::SPCHΔ31* (Fig. 3 and fig. S4, D and E).

To test whether specific S/T residues or the overall number of S/T sites were important for SPCH regulation, we made additional combinations of S/T → A changes and assayed their ability to induce additional cell divisions. In representative lines from each variant (*21*), the ability to promote excess asymmetric cell division increased as more sites were eliminated (Fig. 3 and fig. S4). These results strongly suggest that multiple P-X-S/T-P sites are biologically important sites for SPCH regulation. Using mass spectrometry, we found evidence of phosphorylation at several of these functionally critical sites (fig. S5).

Elimination of MAPK target sites generated SPCH variants with greater activity, consistent with phosphorylation of the MPKTD having a repressive role. If the MPKTD is solely a negative regulatory domain, then each of the variants

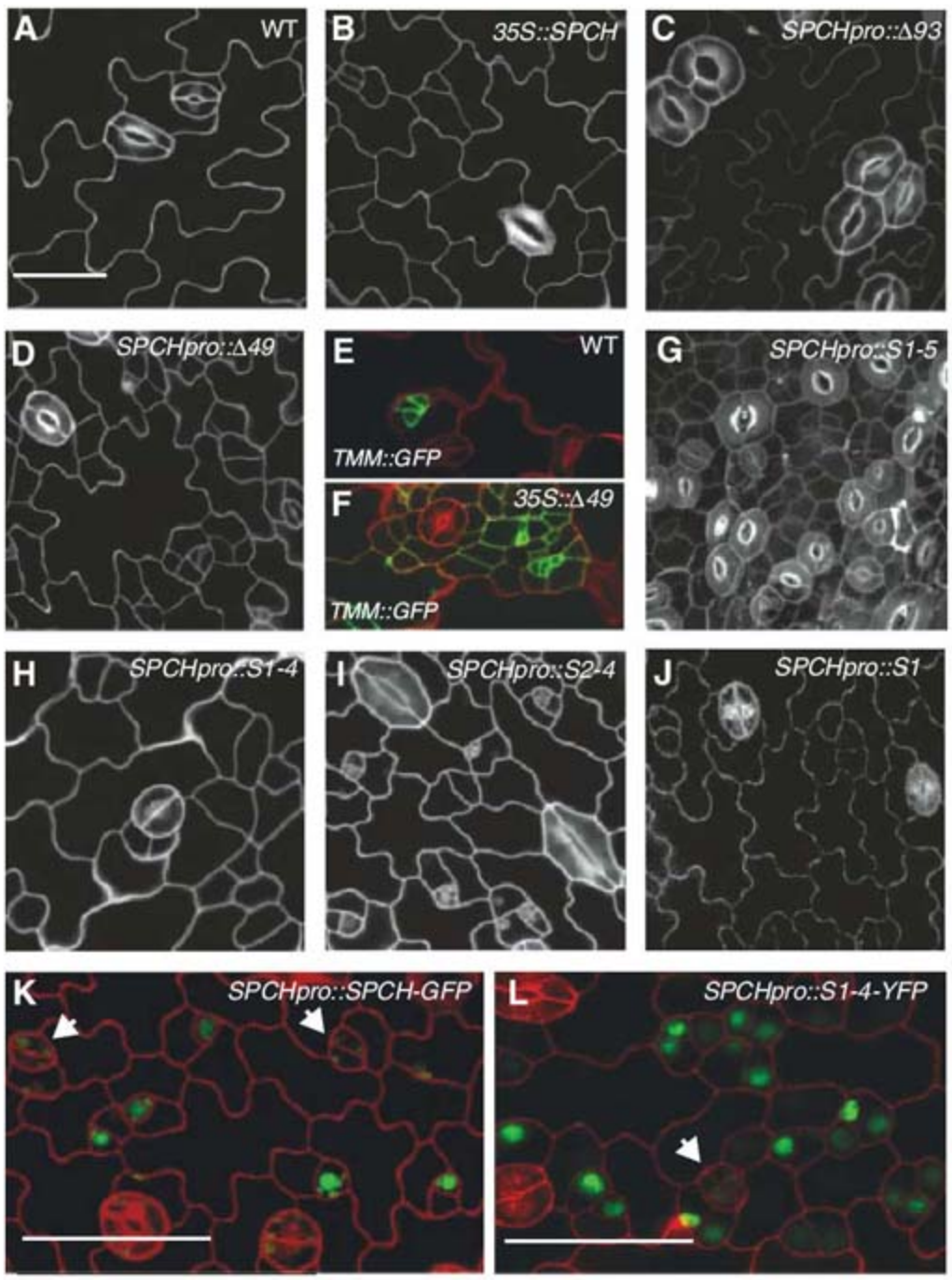

Fig. 2. Confocal images of phenotypes of SPCH variants expressed in plants. (**A** to **D** and **G** to **J**) Confocal images of 7-dpg abaxial cotyledons. Specific genotypes are noted in upper right corner of images. (**E** and **F**) Expression of *TMMpro::TMM-GFP* (green) in *35S::SPCHΔ49* (F) compared to wild-type (WT) control (E). (**K** and **L**) Comparison of expression pattern for full-length SPCH (K) and SPCH variant with four S/T → A substitutions (L) in abaxial leaves 1 and 2 at 11 dpg. SPCH expression in nuclei is shown in green. Note additional SPCH-expressing cells and persistence of SPCH in young guard cells (white arrow) in (L). Images in (A) to (J) are at the same magnification. Scale bars, 50 μm.

should still rescue *spch* mutant phenotypes. We assayed rescue of *spch-3* by MPKTD deletion and S/T → A variants (fig. S6); in the course of this experiment, we found it necessary to refine our criteria for rescue to include not only the production of stomata (the ultimate result of *SPCH* activity) but also the generation of physically asymmetric cell divisions (the immediate consequence of *SPCH* activity), because multiple SPCH variants appeared to separate these two processes. For example, *SPCHpro::SPCH1-4 S/T>A*, *SPCHpro::SPCHΔ49*, and *35S::SPCHΔ49* did not produce stomata but did induce additional asymmetric divisions (figs. S4I and S6). It was possible to trace the failure to rescue *spch* to a single mutation (Ser^{193} → Ala in *SPCHpro::SPCH1 S>A*) (fig. S6), indicating a positive role for phosphorylation in the MPKTD in addition to negative regulatory elements.

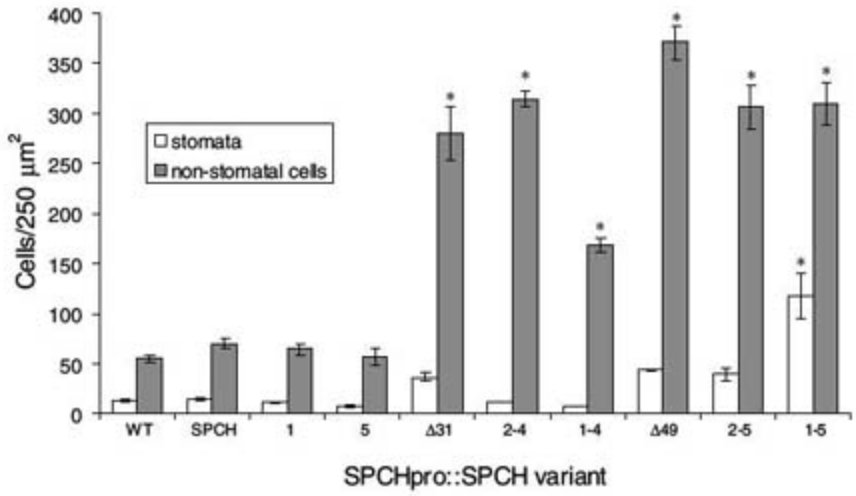

Fig. 3. Production of divisions and stomata by SPCH variants in the wild type. Shown are average numbers of stomata and nonstomatal cells (pavement, meristemoid, and small dividing cells) in 0.25-mm^2 sections of 7-dpg abaxial Col cotyledons expressing the indicated SPCH variant with the SPCH promoter. Asterisk indicates significant difference from *SPCHpro::SPCH* phenotype [joint confidence coefficient $P = 99\%$ (*21*)]. Error bars are ±SE.

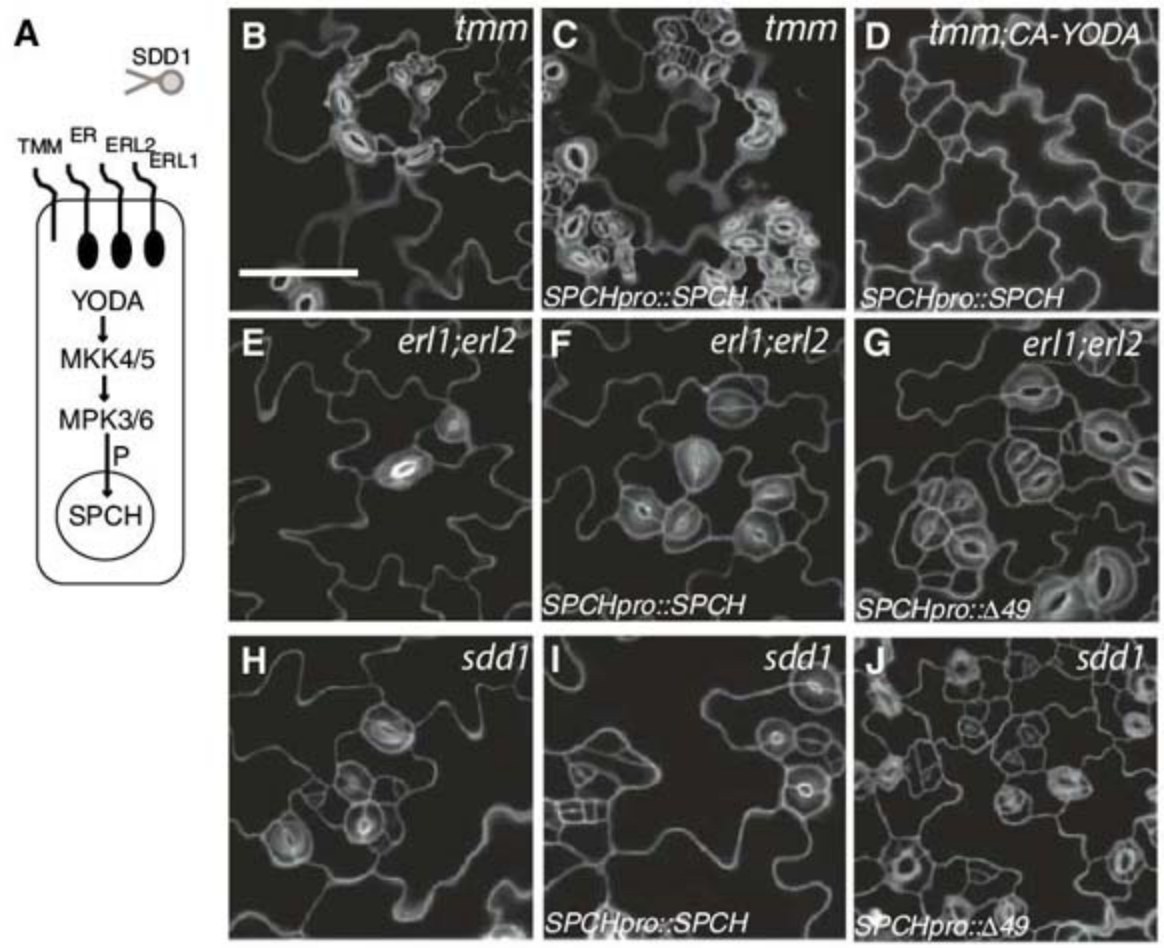

Fig. 4. Effects of endogenous stomatal regulators on SPCH function. (**A**) Scheme of known stomatal regulatory pathway (P, phosphorylation). (**B** to **D**) Suppression of *tmm-1*–mediated enhancement of *SPCHpro::SPCH* phenotypes by *CA-YODA*. (B) Baseline of *tmm-1* clustered stomata. (C) Enhanced clusters in *SPCHpro::SPCH; tmm-1*. (D) Block in excess stomatal production by *CA-YODA* in *SPCHpro::SPCH; tmm-1*. (**E** to **G**) Enhancement of SPCH activity in *erl1;erl2* mutant background. (E) *erl1;erl2* with no stomatal clusters, (F) *SPCHpro::SPCH; erl1;erl2*, and (G) *SPCHpro::SPCHΔ49; erl1;erl2* all result in a statistically significant increase in the stomatal density and fraction of stomata in clusters. (**H** to **J**) Lack of enhancement of SPCH by *sdd1*. (H) *sdd1* mutants exhibit pairing of stomata and increased density. Expression of *SPCHpro::SPCH* (I) or *SPCHpro::SPCHΔ49* (J) in *sdd1* does not enhance the *sdd1* stomatal overproduction phenotype.

Results with the S/T → A SPCH variants suggested that negative regulation by phosphorylation can be a mode of SPCH regulation. If the known stomatal regulators and MAPK components are endogenous regulators, then SPCH activity should be enhanced when these regulators are eliminated by mutation. Our results support this hypothesis; *SPCHpro::SPCH-GFP* expression in a *tmm-1* background yielded a massive overproduction of stomata instead of a subtle increase in epidermal cell divisions (*2*) (Fig. 4, B and C). This stomatal overproliferation phenotype could be suppressed by expressing *CA-YODA* in *SPCHpro::SPCH-GFP;tmm-1* plants (Fig. 4D). We further tested the effects of known stomatal regulators on SPCH behavior by expressing *SPCHpro::SPCH* and *SPCHpro::SPCHΔ49* in backgrounds with mutations in either *MPK3* or *MPK6* and in a double mutant of the putative upstream receptor-like kinases *ERL1* and *ERL2*. These backgrounds were specifically chosen because none has a stomatal patterning defect on its own (*10*, *22*). In each MAPK and receptor mutant background, the phenotypic effect of *SPCH* expression was significantly enhanced relative to the wild type, consistent with these proteins being endogenous upstream regulators (Fig. 4, E to G, and fig. S7). As a control for whether the effect on SPCH activity was specific to MAPK-related stomatal regulators, we also expressed the variants in *sdd1*. SDD1 is also a negative regulator of stomatal development but was recently shown to act independently of YODA, TMM, and ER in perception of EPF1 (*8*). There was no statistically significant increase in stomatal production or clustering when *SPCHpro::SPCH* or *SPCHpro::SPCHΔ49* were expressed in *sdd1* (Fig. 4, H to J, and fig. S7, A and B). Taken together, the behavior of SPCH in these mutant backgrounds suggests that members of the established stomatal receptor/MAPK signaling system modulate SPCH activity in vivo. These results do not rule out additional regulators or MAPK pathway members being involved in SPCH regulation. Furthermore, although these results are consistent with TMM, ER-family receptors, and the MAPKs controlling SPCH activity itself, it is also possible that these proteins regulate the behavior of cells produced by SPCH activity.

Eliminating MAPK target sites affects SPCH function and subsequent stomatal development; however, these experiments do not address the mechanism by which phosphorylation affects SPCH. Substrates of MAPK phosphorylation are often associated with changes in localization, stability, or interaction partners (*23*, *24*). All SPCH variants are constitutively nuclear (*2*) (Fig. 2, K and L), which suggests that SPCH phosphorylation does not alter its subcellular localization; however, it is possible that SPCH phosphorylation alters SPCH persistence. A structural hint of this mechanism is the presence of a predicted PEST domain [PESTfind score +7.63 (*21*)] in the SPCH MPKTD (fig. S5). Functionally, elimination of MPKTD phosphorylation sites results in excess SPCH protein as visualized by YFP expression.

Typically, early in leaf development, *SPCHpro::SPCH-YFP* is expressed in many small cells, but fluorescence diminishes as cells become morphologically distinct meristemoids (*2*) (Fig. 2K). Relative to equivalently staged *SPCHpro::SPCH-YFP* plants, *SPCH* variants with strong overproliferation phenotypes displayed increased numbers of YFP-positive cells early (Fig. 2L) and a trend toward increased protein persistence into meristemoid, GMC, and guard cell stages later (Fig. 2L and fig. S8). When expressed in a *CA-YODA* background (in which SPCH was predicted to be phosphorylated), full-length SPCH-GFP was not visible, nor could it promote stomatal development (figs. S2 and S9C). However, GFP-SPCHΔ49, which is missing phosphorylatable residues, was detectable and was able to drive asymmetric divisions (fig. S9D).

SPCH is closely related to two other bHLH transcription factors that control stomatal development. We have shown, however, that a novel domain of SPCH renders it uniquely subject to phospho-regulation by a group of kinases that have been demonstrated to transduce signals downstream of both cell-cell and plant-environment interactions (fig. S10). In general, the domain mediates repression of SPCH and does so in a quantitative manner; the more potential MAPK sites eliminated, the stronger the effect of the SPCH variant on stomatal development. However, one specific residue phosphorylated by MPK6, Ser^{193}, is required positively for activity, which suggests that the MPKTD is the integration site for complex regulatory inputs. The MPKTD is of unknown origin; it is not present in *Arabidopsis* proteins other than SPCH but is found in SPCH homologs from a variety of plant species (fig. S11) (*25*), hence MAPK regulation of a stomatal bHLH is likely to be a widespread regulatory strategy.

SPCH solves a problem intrinsic to MAPK signaling—how is a set of generally used MAPKs recruited to a specific biological event?—by providing the important effector in a spatially and temporally restricted domain. From the perspective of stomatal control, SPCH guards the entry into the stomatal lineage, including the production of self-renewing cells that contribute to later flexibility in epidermal development. This important decision point is likely the target of developmental, physiological, and environmental regulation (*26*, *27*). Coupling the MPK3/6 signaling module to the activity of SPCH provides a unified, yet tunable, output for the complex set of inputs from these sources. Understanding the elements of the MAPK/SPCH regulatory system that coordinate stomatal production with the prevailing climate may allow the production of food or bioenergy crops with the ability to respond and adapt to changes in that climate.

References and Notes

1. K. Ohashi-Ito, D. Bergmann, *Plant Cell* **18**, 2493 (2006).
2. C. A. MacAlister, K. Ohashi-Ito, D. Bergmann, *Nature* **445**, 537 (2007).
3. L. J. Pillitteri, D. Sloan, N. Bogenschutz, K. Torii, *Nature* **445**, 501 (2007).
4. M. M. Kanaoka *et al.*, *Plant Cell* **20**, 1775 (2008).
5. E. D. Shpak, J. M. McAbee, L. J. Pillitteri, K. U. Torii, *Science* **309**, 290 (2005).
6. J. Masle, S. Gilmore, G. Farquhar, *Nature* **436**, 866 (2005).
7. J. A. Nadeau, F. D. Sack, *Science* **296**, 1697 (2002).
8. K. Hara, R. Kajita, K. Torii, D. Bergmann, T. Kakimoto, *Genes Dev.* **21**, 1720 (2007).
9. D. Berger, T. Altmann, *Genes Dev.* **14**, 1119 (2000).
10. H. Wang, N. Ngwenyama, Y. Liu, J. Walker, S. Zhang, *Plant Cell* **19**, 63 (2007).
11. D. C. Bergmann, W. Lukowitz, C. R. Somerville, *Science* **304**, 1494 (2004).
12. C. Jonak, L. Okresz, L. Bogre, H. Hirt, *Curr. Opin. Plant Biol.* **5**, 415 (2002).
13. M. Karin, *Ann. N.Y. Acad. Sci.* **851**, 139 (1998).
14. H. Wang *et al.*, *Plant Cell* **20**, 602 (2008).
15. W. Lukowitz, A. Roeder, D. Parmenter, C. Somerville, *Cell* **116**, 109 (2004).
16. T. Asai *et al.*, *Nature* **415**, 977 (2002).
17. Y. Kovtun, W. Chiu, G. Tena, J. Sheen, *Proc. Natl. Acad. Sci. U.S.A.* **97**, 2940 (2000).
18. J.-X. He, J. Gendron, Y. Yang, J. Li, Z. Wang, *Proc. Natl. Acad. Sci. U.S.A.* **99**, 10185 (2002).
19. T. L. Tootle, I. Rebay, *Bioessays* **27**, 285 (2005).
20. C. Widmann, S. Gibson, M. Jarpe, G. Johnson, *Physiol. Rev.* **79**, 143 (1999).
21. See supporting material on *Science* Online.
22. E. D. Shpak, M. Lakeman, K. Torii, *Plant Cell* **15**, 1095 (2003).
23. S. Joo, Y. Liu, A. Lueth, S. Zhang, *Plant J.* **54**, 129 (2008).
24. M. Ebisuya, K. Kondoh, E. Nishida, *J. Cell Sci.* **118**, 2997 (2005).
25. X. Li *et al.*, *Plant Physiol.* **141**, 1167 (2006).
26. D. Bergmann, F. Sack, *Annu. Rev. Plant. Biol.* **58**, 63 (2007).
27. A. M. Hetherington, F. Woodward, *Nature* **424**, 901 (2003).

28. We thank lab members for discussion and comments on the manuscript, The Carnegie Department of Plant Biology for use of microscopes, and L. Smith for identification of maize homologs. Supported by NSF grant IOS-0544895, U.S. Department of Energy grant DE-FG02-06ER15810, a Terman award, and the Stanford Genome Training Program (National Human Genome Research Institute).

Supporting Online Material

www.sciencemag.org/cgi/content/full/322/5904/1113/DC1
Materials and Methods
SOM Text
Figs. S1 to S11
References

24 June 2008; accepted 14 October 2008
10.1126/science.1162263

Regulatory Genes Control a Key Morphological and Ecological Trait Transferred Between Species

Minsung Kim,[1,3]* Min-Long Cui,[1]* Pilar Cubas,[1,4]* Amanda Gillies,[2] Karen Lee,[1] Mark A. Chapman,[2,5] Richard J. Abbott,[2] Enrico Coen[1]†

Hybridization between species can lead to introgression of genes from one species to another, providing a potential mechanism for preserving and recombining key traits during evolution. To determine the molecular basis of such transfers, we analyzed a natural polymorphism for flowerhead development in *Senecio*. We show that the polymorphism arose by introgression of a cluster of regulatory genes, the *RAY* locus, from the diploid species *S. squalidus* into the tetraploid *S. vulgaris*. The *RAY* genes are expressed in the peripheral regions of the inflorescence meristem, where they promote flower asymmetry and lead to an increase in the rate of outcrossing. Our results highlight how key morphological and ecological traits controlled by regulatory genes may be gained, lost, and regained during evolution.

Changes in regulatory genes have been implicated in a range of evolutionary transitions, operating from the micro- to macro-evolutionary scales (*1*–*3*). These changes have largely been considered as occurring independently within different species. However, it is also possible that interspecific hybridization plays an important role in evolution (*4*). One consequence of such exchanges is that they may allow traits that are lost because of short-term selective pressures to be regained at a later stage. For example, members of the sunflower family (Asteraceae) share a composite flower head, with each head comprising numerous small flowers (florets). In radiate species, the outer florets (ray florets) have large attractive petals, whereas the inner florets (disc florets) tend to be less conspicuous. Loss of the radiate condition has occurred multiple times within the Asteraceae, yielding nonradiate species with only disc florets (*5*). These events often correlate with shifts to higher levels of self-pollination (*6*), which should be favored when mates and/or pollinators occur at low densities (*7*). Partial or complete reversals from the nonradiate back to the radiate condition have been described (*8*), some of which appear to involve interspecific hybridization events (*9*). One explanation for such evolutionary gains and losses is that key regulatory genes control-

[1]Department of Cell and Developmental Biology, John Innes Centre, Colney Lane, Norwich NR4 7UH, UK. [2]School of Biology, University of St. Andrews, St. Andrews KY16 9TH, UK. [3]Faculty of Life Sciences, University of Manchester, Manchester M13 9PT, UK. [4]Centro Nacional de Biotecnología/CSIC, Darwin 3, Campus UAM, 28049 Madrid, Spain. [5]Department of Plant Biology, University of Georgia, Athens, GA 30602, USA.

*These authors contributed equally to this work.
†To whom correspondence should be addressed. E-mail: enrico.coen@bbsrc.ac.uk.

ling the trait can be modified and exchanged between species. To test this idea, we analyzed a well-documented case of interspecific exchange in *Senecio*.

Senecio vulgaris (Groundsel) (Fig. 1A) is an allotetraploid nonradiate species, native to Europe and occurring throughout temperate zones. Radiate forms of *S. vulgaris* (Fig. 1B) arose in the United Kingdom after the introduction of *S. squalidus* (Fig. 1C), a diploid radiate species originating from Sicily. *S. squalidus* was brought to the Oxford Botanic Garden about 300 years ago (*10*), from where it spread. As *S. squalidus* became dispersed throughout the United Kingdom, it crossed with *S. vulgaris*, yielding triploid hybrids (*11*). Although such triploids have low fertility [seed set <0.02% (*9*)], some viable progeny occur as a result of backcrosses with *S. vulgaris*. Further rounds of backcrossing are thought to have led to introgression of the radiate trait into some populations of *S. vulgaris* (*12*, *13*). The resulting polymorphism for the radiate condition in *S. vulgaris* is controlled by a single chromosome region or genetic locus, here termed *RAY* (*14*). Thus, the hypothesized introgression would have involved transfer of the *RAY* locus from *S. squalidus* into *S. vulgaris*.

The *RAY* locus affects floral symmetry. Disc florets have fivefold radial symmetry, whereas ray florets are bilaterally symmetrical (zygomorphic), having enlarged ventral (abaxial) and reduced dorsal (adaxial) petal lobes (Fig. 1D). *CYCLOIDEA* (*CYC*) is a primary gene controlling floral symmetry in *Antirrhinum majus*, a species with entirely zygomorphic flowers (*15*). *CYC* encodes a DNA-binding protein belonging to the TCP family (*16*). Proteins from this family contain a conserved basic helix-loop-helix region that binds DNA (the TCP domain) and have a range of regulatory roles in plant development (*16*, *17*). On the basis of *Antirrhinum* mutant phenotypes, it has been proposed that *CYC*-like genes might also control the development of ray florets in the Asteraceae (*18*). Supporting this theory, ectopic expression of a *CYC-like* gene from *Gerbera hybrida*, *GhCYC2*, has differential effects on ray and disc floret development in this horticultural species (*19*).

To determine whether *CYC-like* genes are involved in the *RAY* locus, homologs were isolated from *S. vulgaris*. RNA in situ hybridizations on radiate plants revealed that two of these genes, termed *RAY1* and *RAY2*, were specifically expressed in ray floret primordia (Fig. 2, A and B). *RAY1* and *RAY2* were expressed in a similar pattern in radiate (*R/R*) and nonradiate (*N/N*) genotypes (Fig. 2, A to D). However, the signal appeared to be stronger in *N/N* compared with *R/R*. This difference was confirmed by the expression levels in RNA from young flower heads (Fig. 2E). Stronger expression of the *N* alleles was also seen in RNA from *N/R* heterozygotes, suggesting that it reflects cis-regulatory changes (Fig. 2E). Phylogenetic analysis showed that *RAY1* and *RAY2* belong to a subfamily of *TCP* genes that include genes known to control flower asymmetry (clade in orange, Fig. 2F). *RAY1* and *RAY2* arose by a duplication event ~30 million years ago (*20*) that occurred early in the evolution of the Asteraceae, before divergence of *Helianthus*, *Gerbera*, and *Senecio* but after divergence of the Asteraceae from the Lamiales (Fig. 2F). *RAY2* appears to be orthologous to *GhCYC2* from *Gerbera*, which is also expressed preferentially in ray florets (*19*).

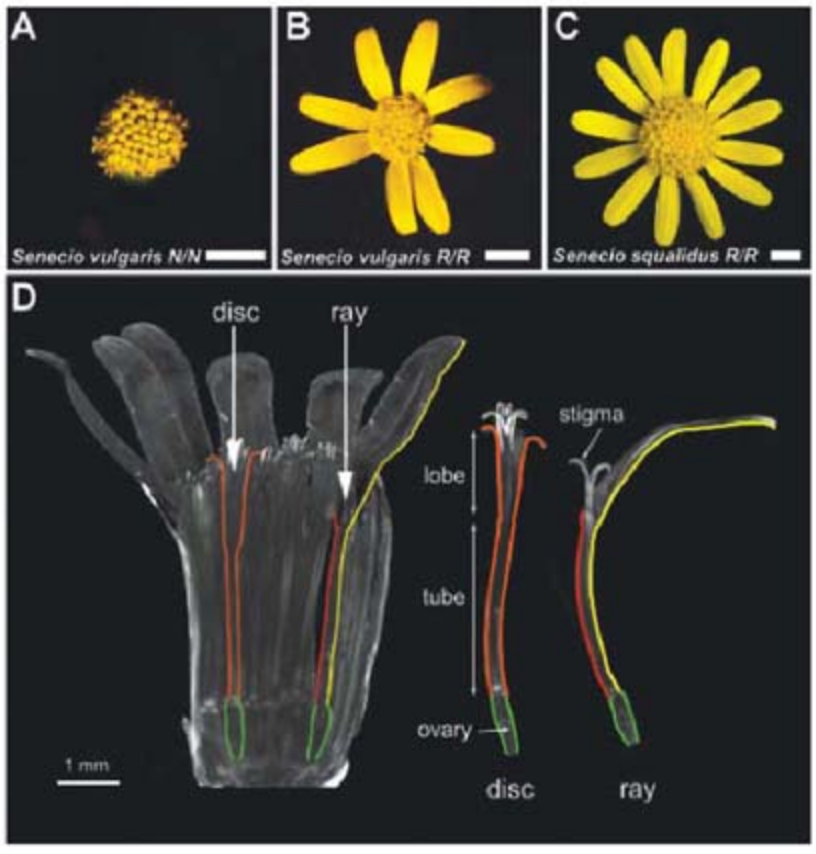

Fig. 1. Flower head of nonradiate *S. vulgaris* (**A**), radiate *S. vulgaris* (**B**), and *S. squalidus* (**C**). Scale bars, 3 mm. (**D**) Section through a flower head and two individual florets taken by optical projection tomography. Disc floret petals are outlined in orange, whereas ray floret petals are outlined in red (dorsal) or yellow (ventral).

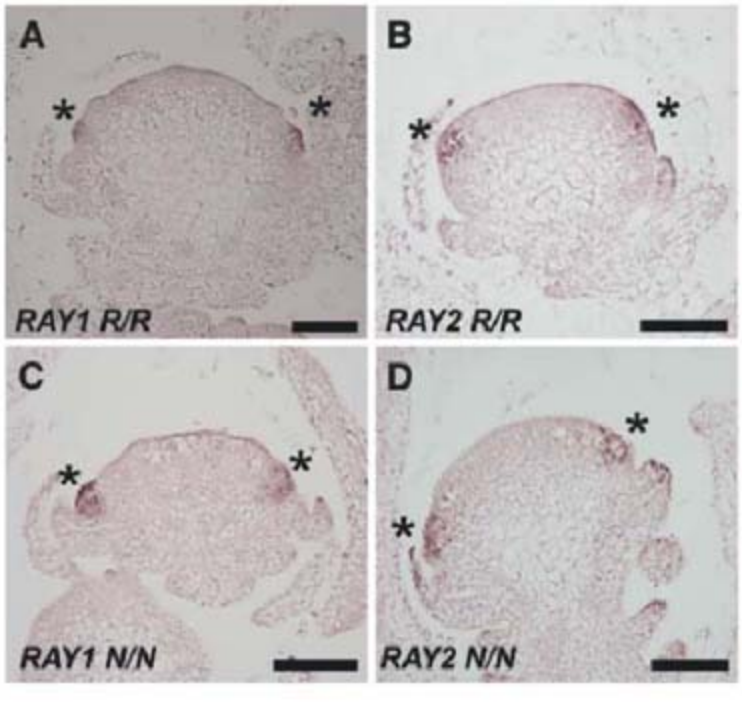

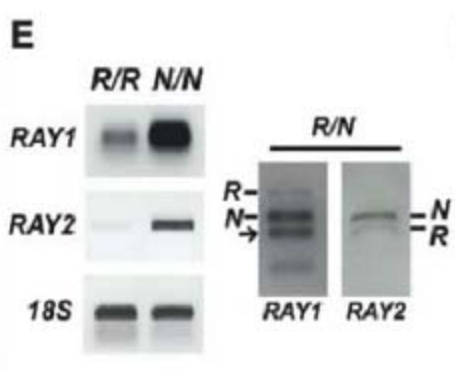

Fig. 2. (**A**) Expression pattern of *RAY1* in a longitudinal section of a developing radiate (*R/R*) flower head. (**B**) Expression of *RAY2* in radiate form. (**C**) Expression of *RAY1* in nonradiate (*N/N*) form. (**D**) Expression of *RAY2* in nonradiate form. In all cases, *RAY1* and *RAY2* are expressed in the outer floret primordia (marked by *). Scale bars, 100 μm. (**E**) Semiquantitative reverse transcription polymerase chain reaction (RT-PCR) showing *RAY1* and *RAY2* expression in young flower heads of *R/R*, *R/N* and *N/N* genotypes. A common band for *R* and *N* is indicated with an arrow in the *R/N* genotype. 18S RNA control is also shown. (**F**) Phylogenetic relationships between *RAY1*, *RAY2*, and a sample of other genes from the TCP family on the basis of a maximum likelihood analysis of amino acid sequences. *RAY1* and *RAY2* belong to a clade with *CYC* and *DICH*, which control floral symmetry in *Antirrhinum* (*15*). Bootstraps of 500 replicates (where greater than 50%) are shown. Species abbreviations and GenBank accession numbers are given in (*30*).

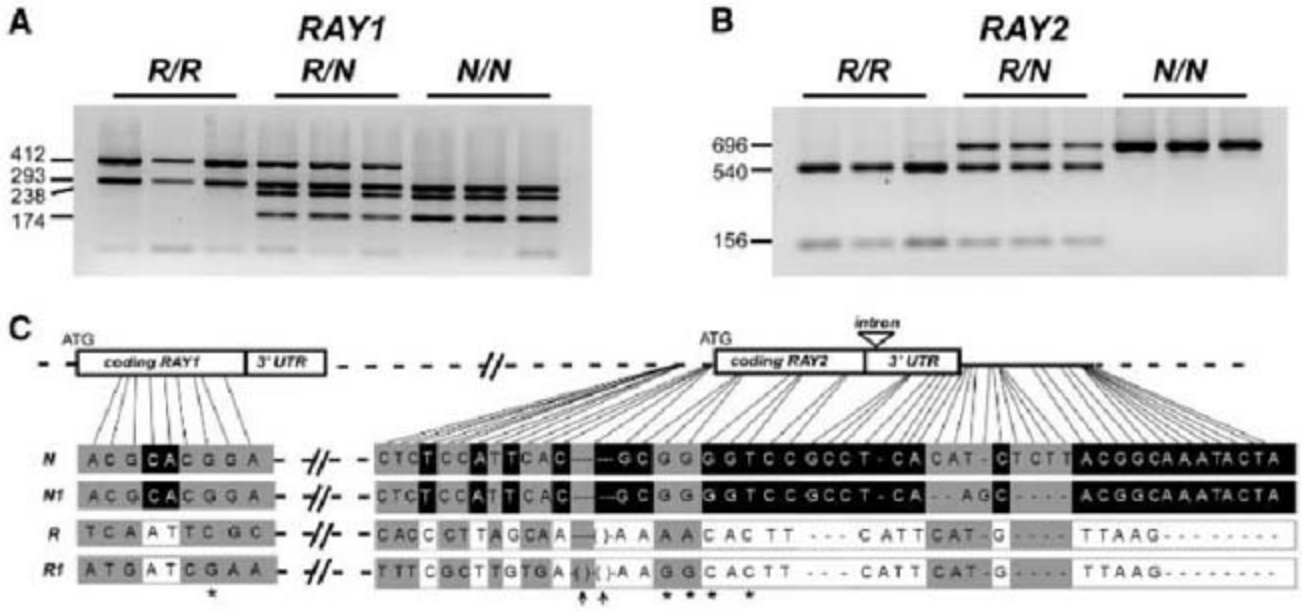

Fig. 3. (**A**) *RAY1*: a 412-bp band that cosegregates with *R* and a 238-bp and a 174-bp band with *N* in an F2 population. (**B**) *RAY2*: a 540-bp and a 156-bp band that cosegregate with *R* and a 696-bp band with *N*. PCR products of *RAY1* and *RAY2* coding regions were digested with *TaqI* and *EcoRI*, respectively. (**C**) Variable sites at *RAY1* and *RAY2* in and around the coding regions for the four haplotypes *N, N1, R*, and *R1*. Polymorphisms that are diagnostic for *N/N1* versus *R/R1* haplotypes are shown surrounded by black and white, respectively. All other polymorphisms are highlighted in gray. Nucleotide polymorphisms that cause amino acid changes are indicated with asterisks. Positions of deletions of TAAGGAAATCCAAACCCCA and ATAGAAA in the *RAY2-R1* haplotype are marked with arrows.

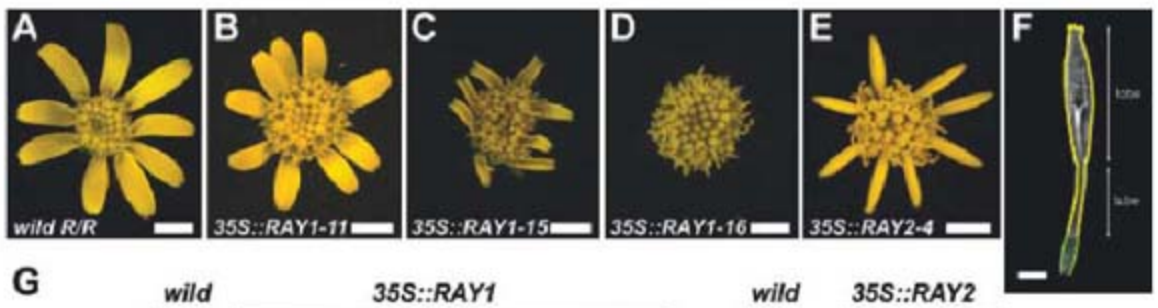

Fig. 4. (**A**) Flower-head phenotypes of *RR* nontransgenic control plant. (**B**) Flower head with slightly short rays from a transgenic plant overexpressing an internal fragment of *RAY1 N* allele coding sequences in a radiate (*R/R*) *S. vulgaris* background. (**C**) Flower head from a *RAY1* transgenic, as in (B), with very short ray florets. (**D**) Flower head from a *RAY1* transgenic, as in (B), giving no ray florets. (**E**) Flower head from a transgenic overexpressing the *RAY2 N* allele coding sequences in a radiate (*R/R*) *S. vulgaris* background, giving tubular ray florets. (**F**) Section through a ventralized ray floret, color-coded as in Fig. 1D. All transgenics are T1 generation, obtained by self-pollinating the primary transformants. (**G**) Semiquantitative RT-PCR showing expression levels of *RAY1* and *RAY2* in the transgenics, together with controls for 18S RNA and the kanamycin resistance gene (*NPTII*). R, normal radiate head; N, nonradiate or discoid head; SS, slightly short rays; S, short rays; VS, very short rays; T, tubular rays with ventralized petals. Scale bars, 2 mm [(A) to (E)] and 1 mm (F).

To determine whether *RAY1* or *RAY2* map to the *RAY* locus, their sequence was determined for parental radiate (*R/R*) and nonradiate (*N/N*) plants, allowing genotype-specific CAPS (cleaved amplified polymorphic sequences) to be designed (Fig. 3, A and B). Genotyping an F2 population derived from these parents revealed that both *RAY1* and *RAY2* segregated with flowerhead phenotype, and we observed no recombinants in more than 700 plants. Linkage between *RAY1* and the *RAY* locus was further confirmed by bulk segregant analysis on *R/R* and *N/N* genotypes, and no recombinants were observed out of 2800 chromosomes. CAPS were also used to genotype accessions of radiate and nonradiate forms from various locations in the United Kingdom (table S1). In all cases, the *RAY1* and *RAY2* genotypes matched the phenotype, confirming a tight association with each other and with the *RAY* locus. This was further confirmed by sequencing the *RAY* genes from several U.K. *S. vulgaris* accessions: All sequences from *R/R* genotypes were identical, while two minor variants were found among *N/N* genotypes, termed *N* and *N1* (Fig. 3C). Thus, both *RAY1* and *RAY2* are tightly linked and associated with *RAY*, and we were able to define three haplotypes: *N, N1*, and *R*. Because the radiate condition in *S. vulgaris* is thought to have originated from *S. squalidus*, *RAY1* and *RAY2* were also sequenced from various U.K. accessions of *S. squalidus*. This revealed two haplotypes, one identical to the *R*-haplotype of *S. vulgaris* and another that was a variant of *R* and was termed *R1* (Fig. 3C and table S1). These results provide molecular proof that the radiate form of *S. vulgaris* arose through hybridization with *S. squalidus* plants and show that the *R*-haplotype was introgressed through this process.

Comparing the sequences of the haplotypes revealed several differences between *N/N1* and *R/R1* (Fig. 3C and fig. S1A). No diagnostic amino acid substitutions were found for *RAY1*, whereas two amino acid substitutions (S to F, D to E) were associated with the *N/N1* alleles of *RAY2*. The substitutions found in the *N* and *N1* alleles of *RAY2* were also found in the radiate species *S. vernalis* and *S. glaucus* (fig. S1B), making it unlikely that they are responsible for the nonradiate condition. Several diagnostic differences were also found in the 5′ and 3′ noncoding regions. As these represent only a limited sample of flanking sequence, it is likely that further differences would also be found in regions extending further out from the genes. Thus, the *N/N1* and *R/R1* haplotypes have accumulated multiple nucleotide differences since they diverged from their common ancestor and it is likely that the functionally important changes lie outside the *RAY1* and *RAY2* coding regions.

The rapid spread of the radiate trait in *S. vulgaris*, despite the strong reproductive barrier between *S. vulgaris* and *S. squalidus*, suggests that the introgression of the *R* haplotype may have been driven by selection, presumably acting on differences outside the *RAY1* and *RAY2* coding regions. However, testing for selection by analyzing sequence variation at the *RAY* locus is not straightforward because most selection tests assume a single interbreeding population (*21*), whereas introgression of *R* involved exchange between two divergent species separated by a major reproductive barrier.

As a further test of whether *RAY1* and *RAY2* play a role in ray floret development, we transformed radiate *S. vulgaris* with two constructs, both of which are driven by the constitutive 35S promoter (the radiate background was chosen because *N* is semidominant and is thought to

represent the derived condition). Expression of an internal fragment of the *RAY1* coding region (*N* allele) that includes the conserved TCP and R domains, yielded 10 independent transformants. Five of these plants produced slightly shorter ray florets (Fig. 4, A and B), three produced very short ray florets (Fig. 4C), and two had only disc florets (Fig. 4D), resembling nonradiate plants. These results suggest that overexpression of *RAY1* is repressing ray floret development, consistent with the higher levels of *RAY1* expression observed in *N/N* genotypes. However, the level of transgene expression did not correlate in a simple manner with the severity of the phenotype; transgenics with slightly short ray florets had higher levels of expression than the discoid transgenics (Fig. 4G). There was also no correlation with the endogenous levels of *RAY1* gene expression, because these levels were similar in transgenics with different phenotypes (fig. S1D). The variation in transgenic phenotype may reflect differences in the pattern of transgene expression, posttranscriptional interactions with the internal *RAY1* fragment used in the transformations, or perhaps promotive as well as inhibitory effects of *RAY1* on ray floret development. Whatever the explanation, the results indicate that *RAY1* plays a critical part in controlling ray versus disc floret identity.

Expression of the entire *RAY2* coding region (*N* allele) in the radiate background produced tubular ray florets in three independent transgenics (Fig. 4E). All petal lobes in these florets resembled the long ventral (abaxial) petal lobes of normal ray florets (Fig. 4, E and F), which suggests that *RAY2* is involved in promoting ventral identity in ray florets. Unlike ectopic expression of *GhCYC2* in *Gerbera hybrida* (*19*), disc floret development was not modified by expression of *RAY2*. This difference may reflect the fact that the innermost florets in *Gerbera hybrida* are not fully radially symmetrical (*19*) and may have some raylike character even in untransformed horticultural varieties.

We conclude that the *RAY* locus comprises a cluster of *CYC-like* genes that have played a key role in the evolution of the radiate condition. Radiate development in the Asteraceae can be compared to the functionally analogous process controlling the development of individual flowers. For both systems, peripheral expression of regulatory genes is involved in establishing the identity of the attractive organs—*CYC* genes for radiate heads and MADS box genes for the flower (*22*–*24*). The main difference is that for radiate heads, peripheral expression is organized with respect to the inflorescence apex, whereas for floral organ identity it is organized in relation to the floral apex. Dorsoventral asymmetry within individual flowers is also established in relation to the inflorescence apex (*18*, *25*). Thus, the ability of *CYC* genes to respond to a basic prepattern, centered on the inflorescence apex, could have led to their co-option and involvement in a key evolutionary innovation in the Asteraceae: radiate development.

The subsequent loss of the radiate condition in lineages of the Asteraceae most likely reflects tradeoffs involved in the evolution of breeding systems. Self-fertilization allows reproductive assurance under conditions where mates and/or pollinators are absent or occur at low densities (*7*) and may be favored, therefore, in colonizing and weedy species, such as *S. vulgaris* (*26*, *27*), despite barriers imposed by inbreeding depression (*28*) and pollen discounting (*29*). However, a self-fertilization strategy may impose long-term limitations on responding to changing environmental conditions. Reintroduction of genes that promote outcrossing may therefore allow a self-pollinating species to revert and prevent extinction in the longer term. Our results therefore highlight the interplay between regulatory genes, development, and life history, and show how gene transfers between species may play an important part in the evolution of key ecological and morphological traits.

References and Notes

1. S. B. Carroll, J. K. Grenier, S. D. Weatherbee, *From DNA to Diversity: Molecular Genetics and the Evolution of Animal Design* (Blackwell Scientific, Malden, MA, 2001).
2. J. Doebley, A. Stec, L. Hubbard, *Nature* **386**, 485 (1997).
3. D. L. Stern, *Nature* **396**, 463 (1998).
4. M. L. Arnold, *Evolution Through Genetic Exchange* (Oxford Univ. Press, Oxford, 2006).
5. J. Q. Liu, Y. J. Wang, A. L. Wang, O. Hideaki, R. J. Abbott, *Mol. Phylogenet. Evol.* **38**, 31 (2006).
6. D. F. Marshall, R. J. Abbott, *Heredity* **52**, 331 (1984).
7. C. Goodwillie, S. Kalisz, C. G. Eckert, *Annu. Rev. Ecol. Evol. Syst.* **36**, 47 (2005).
8. C. A. Stace, *Heredity* **39**, 383 (1977).
9. A. J. Lowe, R. J. Abbott, *Am. J. Bot.* **87**, 1159 (2000).
10. S. A. Harris, *Watsonia* **24**, 31 (2002).
11. D. F. Marshall, R. J. Abbott, *Heredity* **45**, 133 (1980).
12. R. J. Abbott, P. A. Ashton, D. G. Forbes, *Heredity* **68**, 425 (1992).
13. R. Ingram, J. Weir, R. J. Abbott, *New Phytol.* **84**, 543 (1980).
14. A. H. Trow, *J. Genet.* **2**, 239 (1912).
15. D. Luo, R. Carpenter, C. Vincent, L. Copsey, E. Coen, *Nature* **383**, 794 (1996).
16. P. Cubas, N. Lauter, J. Doebley, E. Coen, *Plant J.* **18**, 215 (1999).
17. D. G. Howarth, M. J. Donoghue, *Proc. Natl. Acad. Sci. U.S.A.* **103**, 9101 (2006).
18. E. S. Coen *et al.*, *Philos. Trans. R. Soc. London Biol. Sci.* **350**, 35 (1995).
19. S. K. Broholm *et al.*, *Proc. Natl. Acad. Sci. U.S.A.* **105**, 9117 (2008).
20. M. A. Chapman, J. H. Leebens-Mack, J. M. Burke, *Mol. Biol. Evol.* **25**, 1260 (2008).
21. F. Tajima, *Genetics* **123**, 585 (1989).
22. M. Egea-Cortines, H. Saedler, H. Sommer, *EMBO J.* **18**, 5370 (1999).
23. T. Jack, L. L. Brockman, E. M. Meyerowitz, *Cell* **68**, 683 (1992).
24. E. M. Kramer, V. F. Irish, *Nature* **399**, 144 (1999).
25. J. I. Clark, E. S. Coen, *Plant J.* **30**, 639 (2002).
26. H. G. Baker, *Evolution* **9**, 347 (1955).
27. G. L. Stebbins, *Am. Nat.* **91**, 337 (1957).
28. D. Charlesworth, B. Charlesworth, *Annu. Rev. Ecol. Syst.* **18**, 237 (1987).
29. K. E. Holsinger, *Am. Nat.* **138**, 606 (1991).
30. Materials and methods are available as supporting material on *Science* Online.

31. We thank C. Walton for critical discussion. Supported by EMBO and HFSP long-term fellowship (M.K.), BBSRC grant BB-D017742 (M.C.), BBSRC grant G10929 (R.J.A.) and NERC/S/A/2000/03636 studentship (M.A.C.). GenBank accession numbers for *RAY1* and *RAY2* are FJ356698 to FJ356704.

Supporting Online Material

www.sciencemag.org/cgi/content/full/322/5904/1116/DC1
Materials and Methods
Fig. S1
Table S1
References

7 August 2008; accepted 7 October 2008
10.1126/science.1164371

New Products Focus: Automation

Culture Sample Barcode Labeler

The Labelmaster II is an automated system for labeling and organizing culture media samples in clinical, food, and pharmaceutical testing laboratories. Designed to print and affix labels to petri dishes, the pneumatic system allows up to a thousand plates per hour to be processed and sorted accurately. An optional storage unit increases this capacity to 1,900. Labels are printed and applied directly to the underside edge of the sample plates, which are then stacked and sorted one by one. Applying the label in this way allows automatic plate readers to be used, protects the barcode from scratches and spills, and ensures the label remains attached to the base containing the sample, should the lid become dislodged.

Don Whitley Scientific
For information +44-(0)-1274-595-728
www.dwscientific.co.uk

Personal Automation System

The Maxwell 16 Flexi Method Firmware features a new software system that provides users with flexibility and control of automated instrument operation. The new functionality helps research labs develop and optimize instrument methods to maximize performance for unique sample types and address specific application requirements. The Maxwell 16 System with the Flexi Method Firmware delivers flexible results from diverse sample types; controls key aspects of instrument operation; simplifies workflow with fully integrated prefilled cartridges and preprogrammed protocols; and requires only as much space as a laptop computer. The system can simultaneously purify up to 16 samples without user intervention.

Promega
For information 608-274-4330
www.promega.com

Baculovirus Titer System

A novel titration system, deltaTITER enables researchers to accurately quantify the amount of baculovirus in a sample in just one hour. The kit offers a significant five-day time saving and accuracy benefits compared with the traditional method of plaque assay, which requires skilled personnel and often gives variable results. Measurement of baculovirus titer is an important workflow component for protein expression, in both research and production laboratories. The automated kit is based on a proprietary buffer system, and is designed to be used with deltaDOT's high-performance capillary electrophoresis tool, the Peregrine.

deltaDOT
For information +44-(0)-207-594-1001
www.deltadot.com

Liquid Handling Module

A new Liquid Handling Module extends the functionality of the ArrayScan VTI HCS Reader. The combination of synchronous dispensing-while-imaging capability, kinetic image capture, a range of image analysis algorithms, and "on-the-fly" processing allows the real-time capture of cellular phenotypes and rapid biological responses. Multiple aspirate/dispense options enable dye loading, media replacement, incubation, and stimulus addition to be fully automated. The Cellomics ArrayScan VTI with Liquid Handling Module provides an automated solution for pharmacological studies, including G protein-coupled receptor biology, cell pathway analysis, compound pharmacology, and in vitro toxicology. Compatible with 96-well and 384-well plates, the module makes use of disposable tips with a dispensing volume range of 3 µl to 200 µl.

Thermo Fisher Scientific
For information 905-332-2000
www.thermofisher.com

Magnetic Particle Processors

The MagMAX Express platform is an automated system for nucleic acid isolation that incorporates the rapid, reliable, and cost-effective magnetic bead-based extraction of nucleic acids. MagMAX Isolation Kits extract both genomic and viral nucleic acid from diverse sample matrices, with products available for gene expression analysis, small RNA research, and microarray profiling.

Applied Biosystems
For information 800-327-3002
www.appliedbiosystems.com

Vial Barcode Labeler

The Label X 2D barcode labeler is a stand-alone unit designed to accommodate a wide range of glass vials. This semiautomated labeler applies barcode labels to the bottom of vials and features a compact footprint. The labeler is equipped with interchangeable manifolds so it is simple to change between sample vials without the use of tools. Manifold options include eight, 24, and 96 vials, ranging in diameter from 6.5 mm to 28 mm. It is pneumatically operated and requires no electrical connection, applying up to 96 labels in less than 20 seconds.

MatriCal
For information 509-343-6225
www.matrical.com

Electronically submit your new product description or product literature information! Go to **www.sciencemag.org/products/newproducts.dtl** for more information.

Newly offered instrumentation, apparatus, and laboratory materials of interest to researchers in all disciplines in academic, industrial, and governmental organizations are featured in this space. Emphasis is given to purpose, chief characteristics, and availabilty of products and materials. Endorsement by *Science* or AAAS of any products or materials mentioned is not implied. Additional information may be obtained from the manufacturer or supplier.